



**HAL**  
open science

**PROGRESSIVE STRAIN LOCALIZATION AND  
FLUID FOCUSING IN MANTLE SHEAR ZONES  
DURING RIFTING: PETROSTRUCTURAL  
CONSTRAINTS FROM THE ZABARGAD  
PERIDOTITES, RED SEA**

Marialine Chardelin, Andrea Tommasi, Jose Alberto Padron Navarta

► **To cite this version:**

Marialine Chardelin, Andrea Tommasi, Jose Alberto Padron Navarta. PROGRESSIVE STRAIN LOCALIZATION AND FLUID FOCUSING IN MANTLE SHEAR ZONES DURING RIFTING: PETROSTRUCTURAL CONSTRAINTS FROM THE ZABARGAD PERIDOTITES, RED SEA. Journal of Petrology, 2024, 65 (8), pp.egae081. 10.1093/petrology/egae081 . hal-04387529v3

**HAL Id: hal-04387529**

**<https://hal.science/hal-04387529v3>**

Submitted on 9 Aug 2024

**HAL** is a multi-disciplinary open access archive for the deposit and dissemination of scientific research documents, whether they are published or not. The documents may come from teaching and research institutions in France or abroad, or from public or private research centers.

L'archive ouverte pluridisciplinaire **HAL**, est destinée au dépôt et à la diffusion de documents scientifiques de niveau recherche, publiés ou non, émanant des établissements d'enseignement et de recherche français ou étrangers, des laboratoires publics ou privés.

Copyright

# Progressive Strain Localization and Fluid Focusing in Mantle Shear Zones during Rifting: Petrostructural Constraints from the Zabargad Peridotites, Red Sea

MÉROPE CHARDELIN <sup>1</sup>, ANDRÉA TOMMASI <sup>1,\*</sup> and JOSÉ ALBERTO PADRÓN-NAVARTA <sup>1,2</sup>

<sup>1</sup>Géosciences Montpellier, CNRS & Université de Montpellier, Pl. E. Bataillon, cc. 060, F-34095 Montpellier, France

<sup>2</sup>Instituto Andaluz de Ciencias de la Tierra (IACT), CSIC, Granada, Spain

\*Corresponding author. Géosciences Montpellier, CNRS & Université de Montpellier, F-34095 Montpellier, France. Tel: +33-467144912. E-mail: andrea.tommasi@umontpellier.fr

This article documents the evolution of pressure and temperature conditions and the successive influence of hydrous melts and aqueous fluids on the operation of extensional shear zones, which exhumed mantle slivers from deep lithospheric or asthenospheric depths, in a rift-to-drift setting. These results are based on a re-analysis of 40 samples from three peridotite massifs of Zabargad island in the northern Red Sea. By integrating high-resolution mapping of the microstructure by electron backscattered diffraction with recent developments in barometry for plagioclase-bearing peridotites and thermodynamic modelling of peridotitic compositions, this study (1) constrains the temporal and spatial evolution of petrological and tectonic processes in the shallow mantle during rifting and (2) documents the presence of melts or aqueous fluids throughout the activity of the shear zones, unravelling substantial feedback between petrological and tectonic processes. Thermobarometry and thermodynamic modelling, constrained by the microstructural observations, document progressive strain localization associated with shearing under decreasing pressure and temperature, from near solidus conditions at > 1 GPa (in the north and central peridotite massifs) or ~ 0.7 GPa (in the southern massif) to < 600°C and < 0.3 GPa in all three massifs. The data substantiate local aqueous fluid saturation in the shear zones. This together with higher contents of hydrous minerals in ultramylonites indicate fluid focusing in the shear zones, with seawater ingress extending to > 10 km depth. The presence of melts or fluids enabled concurrent dislocation and dissolution-precipitation creep, resulting in weakening of the shear zones. However, fluid supply was spatially heterogeneous and likely intermittent, with equilibrium achieved only locally in the ultramylonites. The present study documents therefore how the feedback between progressive strain localization and fluid focusing in extensional shear zones contributes to thinning and exhumation of the mantle during continental rifting and the rift-to-drift transition.

**Key words:** extensional shear zones; mantle exhumation; olivine deformation; fluid-assisted deformation; thermodynamic modeling

## INTRODUCTION

The processes thinning the lithosphere, particularly its mantle section, until complete breakup of a plate and creation of a new divergent plate boundary, are still poorly understood. Traditionally, continental rifting models range from symmetric pure shear to asymmetric simple shear end-members (McKenzie, 1978; Wernicke, 1981). Yet, regardless of the overall symmetry or asymmetry of the rift system, geological and geophysical data from continental margins, especially those exposing mantle rocks at the ocean bottom, favour deformation accommodated by large-scale extensional shear zones as the most effective process for lithospheric thinning (e.g. Boillot et al., 1987; Whitmarsh et al., 2001; Dean et al., 2015). Numerical models that successfully reproduce the geometry of continental margins also generally show mantle thinning and asthenospheric upwelling in response to localized shear deformation in trans-lithospheric extensional shear zones (e.g. Weinberg et al., 2007; Brune et al., 2023). However, we lack observational constraints on the actual geometry of these shear zones in the mantle and on the processes controlling their nucleation and growth. The role of melts and fluids on the thinning of the lithosphere and exhumation of the deep levels of the lithosphere during continental rifting as well as during the transition from rifting to drifting also remains a debated question.

The three peridotite massifs that outcrop in Zabargad (23°36'35"N, 36°11'45"E), a small (3 km<sup>2</sup>) island located within the Zabargad fracture zone, 50 km east of the axis of the Red Sea (Fig. 1a, b), offer an exceptional opportunity to document the evolution of the deformation and petrological processes, such as partial melting, fluid ingress, and fluid-rock reactions, in the mantle during the last stages of continental rifting and the rift-to-drift transition. These peridotite massifs preserve a complete record of the deformation processes and metamorphic and metasomatic reactions involved in the exhumation of mantle slices to very shallow, near seafloor depths (Bonatti et al., 1986; Nicolas et al., 1987; Piccardo et al., 1988). The central and northern massifs are mainly composed of spinel lherzolites, whereas the southern massif is dominantly composed of plagioclase lherzolites (Bonatti et al., 1983, 1986; Nicolas et al., 1987), indicating evolution along different pressure-temperature paths.

Structural mapping and microstructural analysis document that all three massifs are characterized by pervasive foliations and lineations formed under high-temperature conditions, which are overprinted by lower temperature deformation focused in discrete shear zones tens of meters to tens of centimetre wide (Bonatti et al., 1986; Nicolas et al., 1987). The mylonitic foliations in the shear zones are in general slightly oblique to the

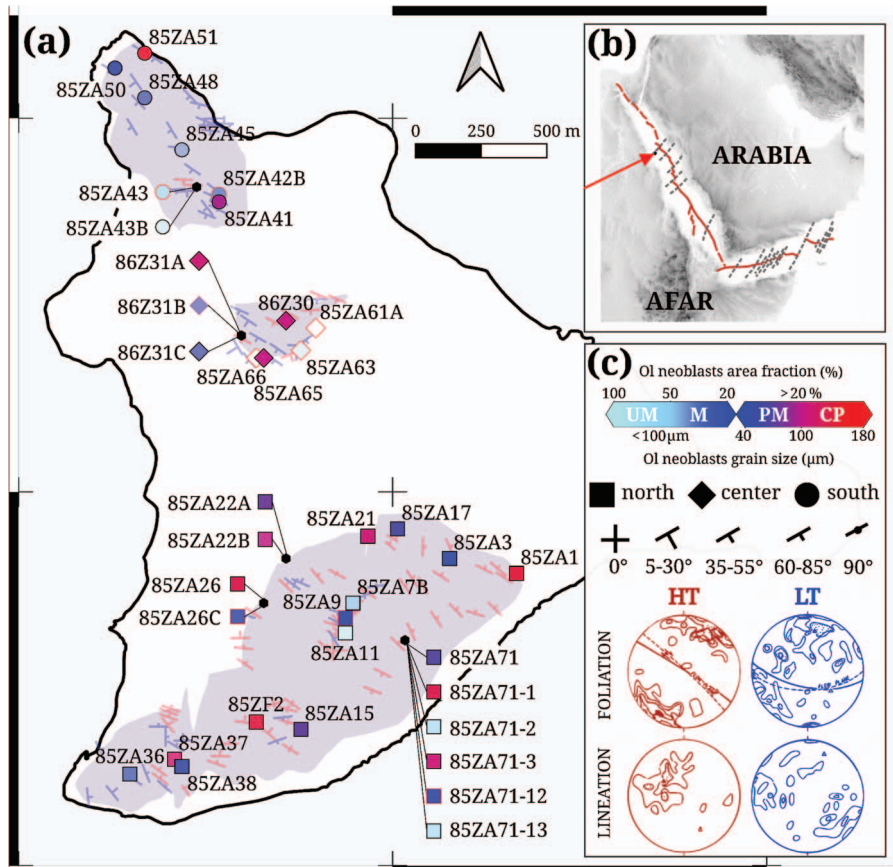


**Fig. 1.** (a) Simplified map of Zabargad showing the spatial distribution of studied samples and the orientation of foliations and lineations for both pervasive and localized deformations in the three peridotite massifs (after Nicolas *et al.*, 1987). Squares, diamonds, and circles indicate samples from the southern, central, and northern massifs, respectively. The red-to-blue colour scale reflects the variations in deformation microstructure. Shades of red indicate samples with coarse porphyroclastic (CP) microstructures associated with the initial pervasive deformation. Shades of purple to light blue indicate samples recording localized deformation in metric to cm-scale shear zones; purple symbols are protomylonites (PM), medium blues, mylonites (M), and light blues, ultramylonites (UM). Point 85ZA71 in the southern massif is a scree, in which loose rocks with highly variable microstructures were collected. (b) Location of Zabargad in the Red Sea (red arrow). (c) Stereographic projections displaying the orientation of the high- and low-temperature foliations and lineations in the three massifs (after Nicolas *et al.*, 1987).

high-temperature ones and the mylonitic lineations have lower plunges (Fig. 1c). Both pervasive and mylonitic foliations have NNW to WNW trends in all three massifs, but they dip mainly towards the SW in the central and northern massifs and towards the NE in the southern massif (Fig. 1a). The orientation of the lineations also differs. In the central and northern massifs, most lineations plunge shallowly towards the E, whereas in the southern massif lineations plunge dominantly towards the NW (Nicolas *et al.*, 1987). The field studies also documented the development of amphibole-rich peridotites within the shear zones. The Central and North peridotite massifs are in direct contact with amphibolite to granulite facies gneisses interpreted as slivers of a thinned continental lower crust and, at the southern limit of the Central massif, the gneisses and peridotites have coherent mylonitic structures (Boudier *et al.*, 1988; Seyler & Bonatti, 1988; Boullier *et al.*, 1997).

Petrological and geochemical studies (Bonatti *et al.*, 1986; Piccardo *et al.*, 1988; Dupuy *et al.*, 1991; Agrinier *et al.*, 1993;) corroborated an evolution under decreasing pressures and temperatures. These studies also documented: (1) petrological evidence for melt impregnation, but depleted LREE patterns in plagioclase peridotites of the southern massif outside the shear zones, (2) diffuse websteritic layering, flat REE patterns in peridotites, and rare Ti-rich pargasite in coarse-grained peridotites

and pyroxenites of the central and northern massifs, indicating variable degrees of metasomatism by alkaline basaltic melts, and (3) marked enrichment in amphiboles with variable major elements and isotopic compositions and strong LREE enrichment in the mylonitic peridotites indicating metasomatism by aqueous fluids in the shear zones in all three massifs, with increasing contribution of seawater in the later stages of deformation.

In this study, we make use of the major advances in the analysis of microstructures brought by the development of automated high-resolution mapping of crystallographic orientations by electron backscattered diffraction (EBSD), as well as of recent developments in barometry of plagioclase-bearing peridotites (Fumagalli *et al.*, 2017) and in thermodynamic modelling of anhydrous and hydrous melting and subsolidus phase relations in peridotitic compositions (Jennings & Holland, 2015; Holland *et al.*, 2018; Tomlinson & Holland, 2021), to better constrain the deformation processes and feedbacks between deformation, melts, and fluids at the different stages of mantle thinning and exhumation recorded in the Zabargad peridotites.

## METHODS

We performed a detailed petrostructural study of 40 samples derived from the three massifs (Fig. 1; Table 1). These samples

**Table 1:** Samples' International Generic Sample Number (IGSN) and field identification, provenance (massif), lithology, microstructural facies, modal composition (area fractions determined from the EBSD maps covering at least 90% of the thin section, uncertainty of  $\pm 1\%$ ), and olivine neoblasts area fraction and size (equivalent grain diameter)

IGSN	SAMPLE IDENTIFIER		MASSIF	LITHOLOGY	MICROSTRUCTURE	MODAL COMPOSITION							OLIVINE NEOBLASTS	
	field ID					Ol	Opx	Cpx	Plg	Sp	Amph	area fraction (%)	grain size ( $\mu\text{m}$ )	
CNRS0000026446	86Z31B	center	websterite	coarse granular	0	33	49	1	0	0	13	-		
CNRS0000026444	86Z30	center	peridotite / websterite layer	coarse porphyroclastic	45	29	17	0	0	0	5	104		
CNRS0000026445	86Z31A	center	peridotite	coarse porphyroclastic	45	34	11	0	1	6	6	115		
CNRS0000026433	85ZA65	center	peridotite / websterite layer	coarse porphyroclastic	51	19	24	0	1	2	2	102		
CNRS0000026447	86Z31C	center	peridotite	mylonite	61	17	0	0	0	19	47	98		
CNRS0000026432	85ZA63	center	websterite	ultramylonite	3	8	42	11	2	31	-	-		
CNRS0000026431	85ZA61A	center	websterite	ultramylonite	0	42	1	0	1	54	-	-		
CNRS0000026434	85ZA66	center	websterite	ultramylonite	0	10	20	0	0	45	-	-		
CNRS0000026424	85ZA42B	north	websterite	coarse granular	0	28	57	2	0	10	-	-		
CNRS0000026430	85ZA51	north	peridotite	coarse porphyroclastic	81	6	0	0	0	11	15	168		
CNRS0000026423	85ZA41	north	peridotite	protomylonite	61	15	2	0	2	17	4	91		
CNRS0000026429	85ZA50	north	peridotite	mylonite	69	16	4	0	1	7	22	96		
CNRS0000026428	85ZA48	north	peridotite	mylonite	66	13	1	0	1	16	35	82		
CNRS0000026427	85ZA45	north	peridotite	mylonite	60	20	2	0	2	15	49	68		
CNRS0000026425	85ZA43	north	pyroxenite	ultramylonite	10	33	0	0	0	55	-	-		
CNRS0000026426	85ZA43B	north	peridotite	ultramylonite	60	9	0	0	0	29	66	71		
CNRS0000026436	85ZA71-12	south	troctolite	coarse granular	22	6	30	38	1	1	18	154		
CNRS0000026417	85ZA26C	south	troctolite	coarse granular	15	19	32	25	0	7	20	87		
CNRS0000026416	85ZA26	south	peridotite / troctolite layer	coarse porphyroclastic	73	19	2	1	0	1	6	143		
CNRS0000026413	85ZA21	south	peridotite	coarse porphyroclastic	66	19	7	4	0	1	6	114		
CNRS0000026435	85ZA71-1	south	peridotite	coarse porphyroclastic	62	19	6	9	0	1	7	143		
CNRS0000026409	85ZA1	south	peridotite	coarse porphyroclastic	62	18	2	13	1	1	7	155		
CNRS0000026439	85ZA71-3	south	peridotite / troctolite layer	coarse porphyroclastic	53	0	33	8	0	3	7	113		
CNRS0000026443	85ZF2	south	peridotite	coarse porphyroclastic	63	24	6	4	0	0	13	152		
CNRS0000026421	85ZA37	south	peridotite	coarse porphyroclastic	57	23	9	7	0	0	19	120		
CNRS0000026411	85ZA15	south	peridotite	protomylonite	63	22	7	5	0	0	4	69		
CNRS0000026419	85ZA31C	south	peridotite / troctolite layer	protomylonite	59	13	11	6	0	9	6	54		
CNRS0000026414	85ZA22A	south	peridotite	protomylonite	72	22	2	0	0	1	8	73		
CNRS0000026440	85ZA71	south	peridotite	protomylonite	53	27	3	0	0	15	12	61		
CNRS0000026412	85ZA17	south	peridotite	protomylonite	60	18	7	9	0	3	13	55		
CNRS0000026415	85ZA22B	south	peridotite	protomylonite	54	24	11	6	0	2	16	98		
CNRS0000026418	85ZA3	south	peridotite / troctolite layer	protomylonite	45	19	21	9	0	3	16	40		
CNRS0000026442	85ZA9	south	troctolite	mylonite	35	10	30	6	0	16	14	108		
CNRS0000026420	85ZA36	south	peridotite / troctolite layer	mylonite	44	31	11	9	0	1	22	72		
CNRS0000026422	85ZA38	south	peridotite	mylonite	64	17	7	4	0	5	22	94		
CNRS0000026441	85ZA7B	south	peridotite	mylonite	52	24	8	9	0	4	39	46		
CNRS0000026438	85ZA71-2	south	peridotite	mylonite	54	15	0	0	0	29	46	37		
CNRS0000026437	85ZA71-13	south	peridotite	ultramylonite	64	24	0	0	0	9	48	36		
CNRS0000026410	85ZA11	south	peridotite	ultramylonite	67	8	1	0	0	21	52	35		



were collected by Françoise Boudier and Adolphe Nicolas during field trips in 1985 and 1986. The field data as well as microstructural data for the entire collection is presented in [Nicolas et al. \(1987\)](#). The composition of the amphiboles, as well as whole-rock Sr, H, and O isotopes, and whole-rock trace-element compositions of part of this collection, including some of the samples studied here, are presented in [Agrinier et al. \(1993\)](#) and [Dupuy et al. \(1991\)](#), respectively.

The microstructures of all samples were analysed by optical microscopy and crystal orientations by EBSD at the thin section scale. For 12 samples, we also performed simultaneous high-spatial resolution EBSD and chemical mapping by energy dispersive X-ray spectroscopy (EDS) of selected areas. Chemical compositions of the major rock-forming minerals were measured by electron probe micro-analyser (EPMA) for 18 samples representative of the different microstructures and modal compositions in the three massifs.

## EBSD data acquisition and processing

Measurement of crystallographic orientations of olivine, pyroxenes, plagioclase, spinel, and amphibole was performed in the Geosciences Montpellier SEM-EBSD facility. EBSD mapping was performed on entire thin sections (at least 90% of the section surface was analyzed) with steps ranging from 7 to 44  $\mu\text{m}$  depending on the average grain size (in all cases, the grains composing >95% of the analysed surface are covered by at least 3 data points) using a JEOL5600 scanning electron microscope (SEM) equipped with a Nordlys II EBSD detector and the AZtecHKL software from Oxford Instruments. Data were acquired with a working distance of 24 mm, a beam current of 10 nA, and an acceleration voltage of 17 kV. For 12 samples representative of the different microstructural facies, higher spatial resolution EBSD and EDS maps with step sizes of 1–12.5  $\mu\text{m}$  were acquired using a field-emission SEM—the CamScan Crystal Probe X500 FE, equipped with the Oxford Symmetry EBSD detector and an UltimMax 100 EDS detector. The phases declared for EBSD indexation were olivine, orthopyroxene, clinopyroxene, spinel, plagioclase, and amphibole (pargasite). In the high-resolution analyses, antigorite, chlorite, calcite, and talc were added to the mineral phase list. The EBSD data was cleaned with the Aztec software by removing wild spikes (isolated measurement points) and replacing the unindexed pixels with the average orientation of their neighbours if at least six neighbours belonged to the same phase and had a consistent orientation.

EBSD data treatment was performed using the MTEX toolbox v.5.10.2 in Matlab (<http://mtex-toolbox.github.io/>; [Bachmann et al., 2010, 2011](#)). Grains were reconstructed using a Voronoi tessellation constrained by the indexed points and a misorientation threshold of 15° to define a grain boundary. Subgrain boundaries are defined with a misorientation threshold of 2°, considering a maximum angular uncertainty in the EBSD data of 1°. Modal compositions were approached as the area fraction occupied by each mineral on the EBSD maps. For better visualization of the microstructures, modal composition and orientation maps are presented in the following with all indexed data, but statistical analysis of the microstructure and crystallographic orientation was performed after removing grains composed of less than three pixels. Boundary grains could not be removed from the analysis, because in some thin sections, some of the boundary grains are coarse porphyroclasts, which represent significant fractions of the mapped area.

Orientation distribution functions (ODFs) describing the crystal-preferred orientations of all minerals were calculated using a 'de la Vallée Poussin' kernel with a halfwidth of 10°. They are displayed as lower hemisphere stereographic projections in which the orientation of the main crystallographic directions: [100], [010], and [001] of each mineral phase is plotted relative to the principal axes of the strain ellipsoid X, Y, and Z, defined based on the observation of the foliation and lineation in the hand samples.

The concentration (intensity) of the CPO of the different minerals was quantified using the dimensionless J-index, which is the volume-averaged integral of the squared orientation densities in the ODF ([Bunge, 1982](#)). The J-index varies from 1 for a uniform orientation distribution, to infinity for a single crystal. In naturally deformed peridotites, the J-index calculated using the same parameters as in the present study typically ranges between 1 (random CPO) and 18, with a median of 4.8 ([Tommasi & Vauchez, 2015](#)). The symmetry of the olivine CPO is characterized using the BA index, which varies between 0 and 1 ([Mainprice et al., 2015](#)). The BA index allows a classification of the olivine CPO symmetry into three types: axial-[010], characterized by a point concentration of [010] and a girdle distribution of [100] (BA-index < 0.35), orthorhombic, characterized by point concentrations of both [100] and [010] (0.35 < BA-index < 0.65), and axial-[100], characterized by a point concentration of [100] and a girdle distribution of [010] (BA-index > 0.65).

Intragranular misorientations, which result essentially from the accumulation of geometrically necessary dislocations, are quantified using the Kernel Average Misorientation (KAM, which is a measure of the mean misorientation around a measurement point), the local misorientation relative to the mean orientation of the grain (Mis2Mean), and the Grain Orientation Spread (GOS, which is the average of the local misorientations relative to the mean orientation of the grain). These data, together with grain sizes and shapes, are the basis for the quantitative analysis of the microstructures. Grains were classified as porphyroclasts (grains predating the deformation) or neoblasts (newly formed grains) based on both their size and internal deformation. The justification for these criteria is that both recrystallization and reactions create new grains (neoblasts) with initially small sizes and very low dislocation densities. Neoblasts are therefore defined as having a GOS < 1° and an equivalent grain size (the diameter of a circle with the same area as the grain) < 400  $\mu\text{m}$  ([Fig. 2](#)). The double threshold assumes that coarse grains with low GOS values are porphyroclasts poorly oriented to deform by dislocation creep. Amphiboles being a secondary phase in the present rock assemblages were classified as neoblasts independently of their GOS or grain size.

To establish a quantitative characterization of the microstructure, we calculated, for each mineral, average values at the thin section scale of the orientation data (J- and BA-indexes, KAM, Mis2Mean, and GOS), as well as area-weighted averages of the equivalent grain size, aspect ratio (the ratio between the long and short axis of the ellipse that best fits the grain), and shape factor (the perimeter of the grain divided by the perimeter of a circle with the same area as the grain, which increases with increasing sinuosity of the grain boundaries). These values were calculated for the entire grain population in the EBSD map and separately for the porphyroclasts and neoblasts. The full dataset is presented in the Supporting Information [Table S1](#).

Paleostresses associated with the different microstructures were estimated based on the olivine neoblasts size using the

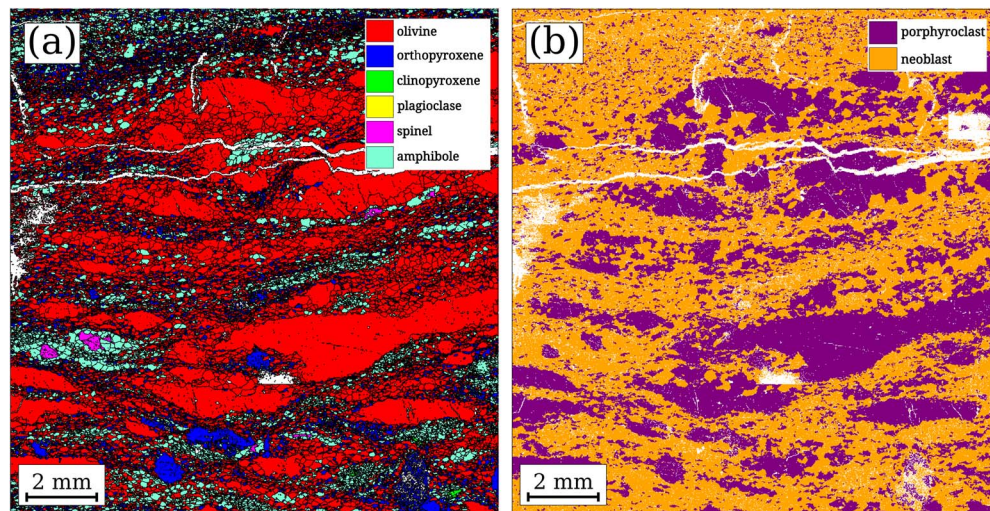


**Fig. 2.** (a) EBSD phase map and (b) map illustrating the separation of porphyroclasts (purple) from neoblasts (orange) based on the double criteria of a grain orientation spread (GOS)  $\geq 1^\circ$  and an equivalent grain diameter  $\geq 400 \mu\text{m}$  in mylonitic peridotite 86Z31C.

Van Der Wal *et al.* (1993) piezometer based on the arithmetic mean of the equivalent neoblast size in each sample using the Python script developed by M. Sánchez-López with a correction for the difference in stress regime between experiments and nature ([https://github.com/marcoalopez/GrainSizeTools/blob/master/DOCS/\\_Paleopiezometry.md](https://github.com/marcoalopez/GrainSizeTools/blob/master/DOCS/_Paleopiezometry.md)). The average olivine neoblast size is estimated over the entire EBSD mapped area, without discriminating between mono- or polymineralic domains, since the presence of other phases tends to be pervasive in the fine-grained domains. Thus, neoblast sizes do not result solely from dynamic recrystallization and were probably also affected by dissolution–precipitation processes. However, as both recrystallization and dissolution–precipitation were active during the entire deformation history, we assume that the stress estimates can be analysed in a qualitative way, as indicators of changes in the strength of the peridotites.

### Mineral chemistry analysis and geothermometry

Major element composition of olivine, orthopyroxene, clinopyroxene, spinel, plagioclase, and amphibole were analysed in 14 samples representative of the different microstructural facies and modal composition range in the three massifs using a Cameca SX100 EPMA at the University of Montpellier. Analytical conditions and the full dataset are presented in the Supporting Information Table S2.

Optical observation of microstructures and EBSD maps were used to identify the equilibrium assemblies associated with the different stages of deformation. EDS maps have been used to determine spatial variations in chemical composition and correlate them with the deformation microstructures. The grains comprising the matrix of coarse-porphyroclastic, protomylonitic, mylonitic, and ultramylonitic peridotites are considered to have progressively equilibrated during the different stages of the deformation that affected the Zabargad peridotites. The cores of coarse porphyroclasts are assumed to have preserved a record of the initial deformation conditions, while the rims of porphyroclasts are presumed to have undergone re-equilibration towards the conditions prevailing during the formation of the matrix. These assumptions guided the collection and analysis of EPMA data. However, given that EPMA analyses are performed on a 2D section of a 3D structure, some of the data collected in the ‘core’ of

a grain as imaged in 2D may be close to a grain boundary in the third dimension and have thereby recorded re-equilibration during the evolution of the system. These data were reclassified as ‘apparent’ cores.

Equilibrium temperatures and pressures for different microstructural assemblies have been calculated using iteratively the Ca in orthopyroxene thermometer of Brey & Köhler (1990) revised by Nimis & Grütter (2010) and the FACE barometer of Fumagalli *et al.* (2017). For samples that do not contain plagioclase or clinopyroxene, the temperature calculation was performed using a pressure of 0.5 GPa, which is the average of the pressure estimates for the other samples. Temperatures were also estimated using the Al–Cr in orthopyroxene thermometer (Witt-Eickschen & Seck, 1991). The two-pyroxene thermometer of Taylor (1998) was also tested, but it produced inconsistent temperatures, probably due to a lack of equilibrium between the two pyroxenes, which is common in systems subjected to extensive reactions with melts or fluids. The uncertainty in the equilibrium pressure and temperature conditions due to spatial variations in the minerals composition within a sample was estimated by considering all possible combinations between core, rim, and matrix analyses for the different minerals in each sample. The results are presented as the median with error bars indicating the dispersion (minimum and maximum values) in each petrographic class.

### Thermodynamical modelling

Phase equilibria and mineral compositions were computed by Gibbs energy minimization using the PerpleX algorithm version 7.0.9 (Connolly, 2005, 2009). Forward thermodynamic modelling was performed in the KNCFMASHTOCr system using the thermodynamic system components:  $\text{K}_2\text{O}-\text{Na}_2\text{O}-\text{CaO}-\text{FeO}-\text{MgO}-\text{Al}_2\text{O}_3-\text{SiO}_2-\text{H}_2\text{O}-\text{TiO}_2-\text{O}_2-\text{Cr}_2\text{O}_3$ . Thermodynamic data for end members are defined based on Holland & Powell (2011). The considered solid solutions models were: olivine (Ol), orthopyroxene (Opx), clinopyroxene (Cpx), garnet (Gt), and spinel (Spl) from (Tomlinson & Holland, 2021), plagioclase (Pl) from Holland *et al.* (2022), clinoamphibole from Green *et al.* (2016), chlorite (Chl) from White *et al.* (2014) with the fclin3 endmember excluded, peridotitic dry melt from Jennings & Holland (2015), and generic hydrous melt from Holland *et al.* (2018).

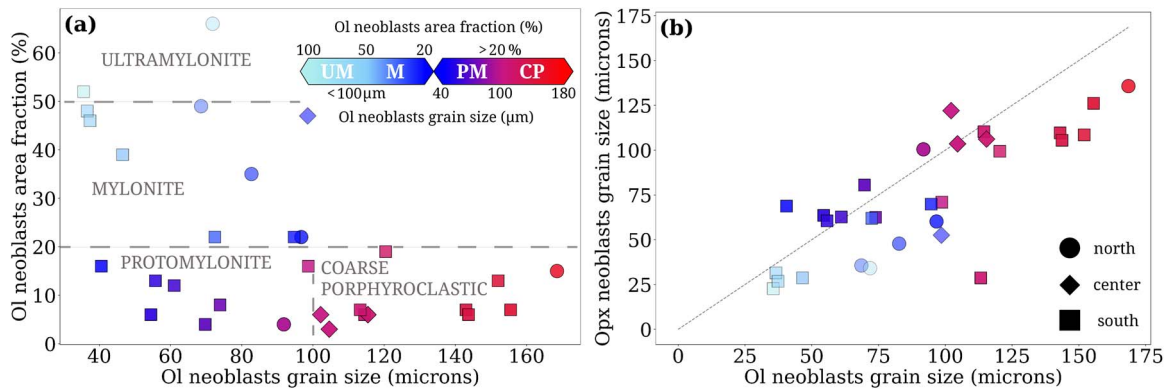


**Fig. 3.** (a) Olivine neoblasts area-weighted mean equivalent grain size versus area fraction (relative to the total olivine area fraction). These two criteria are combined to define the different microstructural facies as indicated in this panel. (b) Olivine neoblasts area-weighted mean equivalent grain size versus orthopyroxene area-weighted mean equivalent grain size. Squares, diamonds, and circles correspond to samples from the southern, central, and northern massifs, respectively. The dashed line in panel (b) marks the 1:1 relation.

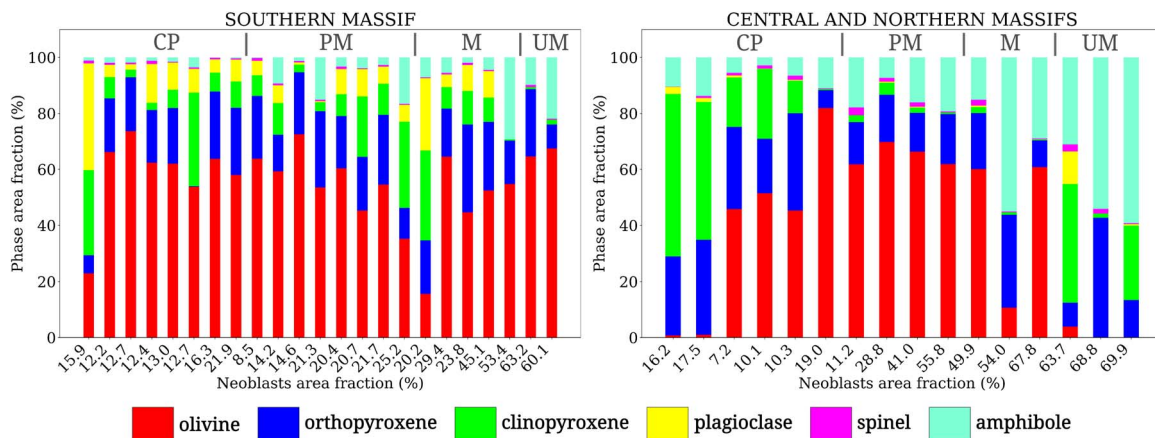


**Fig. 4.** Modal composition of all studied samples as a function of the bulk (all phases) neoblasts area fraction in each sample (value given in the X axis). Samples are classified as a function of the provenance and of the microstructural facies.

## RESULTS

### Microstructures and modal compositions

Based on field observations, Bonatti *et al.* (1986) and Nicolas *et al.* (1987) proposed that the three massifs recorded deformation with progressive strain localization, which allowed the preservation of microstructures formed under decreasing pressure and temperature conditions. To describe this evolution, we classified the microstructures of the peridotites into four facies (Fig. 3). The first, coarse-porphyroclastic peridotites, is composed of peridotites with microstructures typical of deformation at high temperature and low stress conditions. This deformation created the pervasive foliation and lineation in the massifs. The three other microstructural facies are observed in the shear zones. They record reworking under lower temperature conditions of the primary coarse-porphyroclastic microstructure. Increasing finite strains resulted in protomylonites, mylonites, and ultramylonites. Deformation facies are usually defined based on the proportion of neoblasts of all minerals in a rock. However, in the present study, the classification of the microstructures of the peridotites has been defined solely based on the microstructure of olivine (Fig. 3a), because, as discussed later, the evolution of the microstructure of the other major rock-forming minerals was more affected by synkinematic reactions with melts or fluids. Peridotites in which more than 50% of the olivine area is identified as neoblasts are classified as ultramylonites and between 50

and 20% as mylonites. When less than 20% of the olivine is recrystallized, they are classified as coarse-porphyroclastic peridotites if the area-weighted equivalent grain diameter of the olivine neoblasts is larger than 100  $\mu\text{m}$ , or protomylonites, if the area-weighted equivalent grain diameter of neoblasts is lower than 100  $\mu\text{m}$ , suggesting incipient recrystallization under higher stress conditions. Pyroxenites were classified as mylonitic or ultramylonitic when the total neoblast fraction (considering all minerals) in the thin section was >20% or >50%, respectively, and coarse granular otherwise. We describe below the main characteristics of each microstructural facies. However, the evolution of the microstructure is continuous (cf. Fig. 3). Many samples have microstructures intermediate between those of two facies.

Very fertile compositions, characterized by >20 area % of Al-rich phases (clinopyroxene, plagioclase, spinel, or amphibole), predominate in all three massifs independently of the deformation microstructure (Figs 4, S1). High contents of plagioclase (up to 14 area %, Table 1) are only observed in the southern massif, where plagioclase is often the dominant Al-rich phase (Figs 4, 5a, e, 6a). In this massif, the mafic layers have wehrlitic to troctolitic compositions (Fig. 6e). In the northern and central massifs, the pyroxenites are spinel websterites and plagioclase is only occasionally observed rimming spinel, except in an ultramylonitic pyroxenite (Fig. 4, Table 1).

Some studied samples are heterogeneous, containing diffuse layers of spinel websterite (in the northern and central massifs,



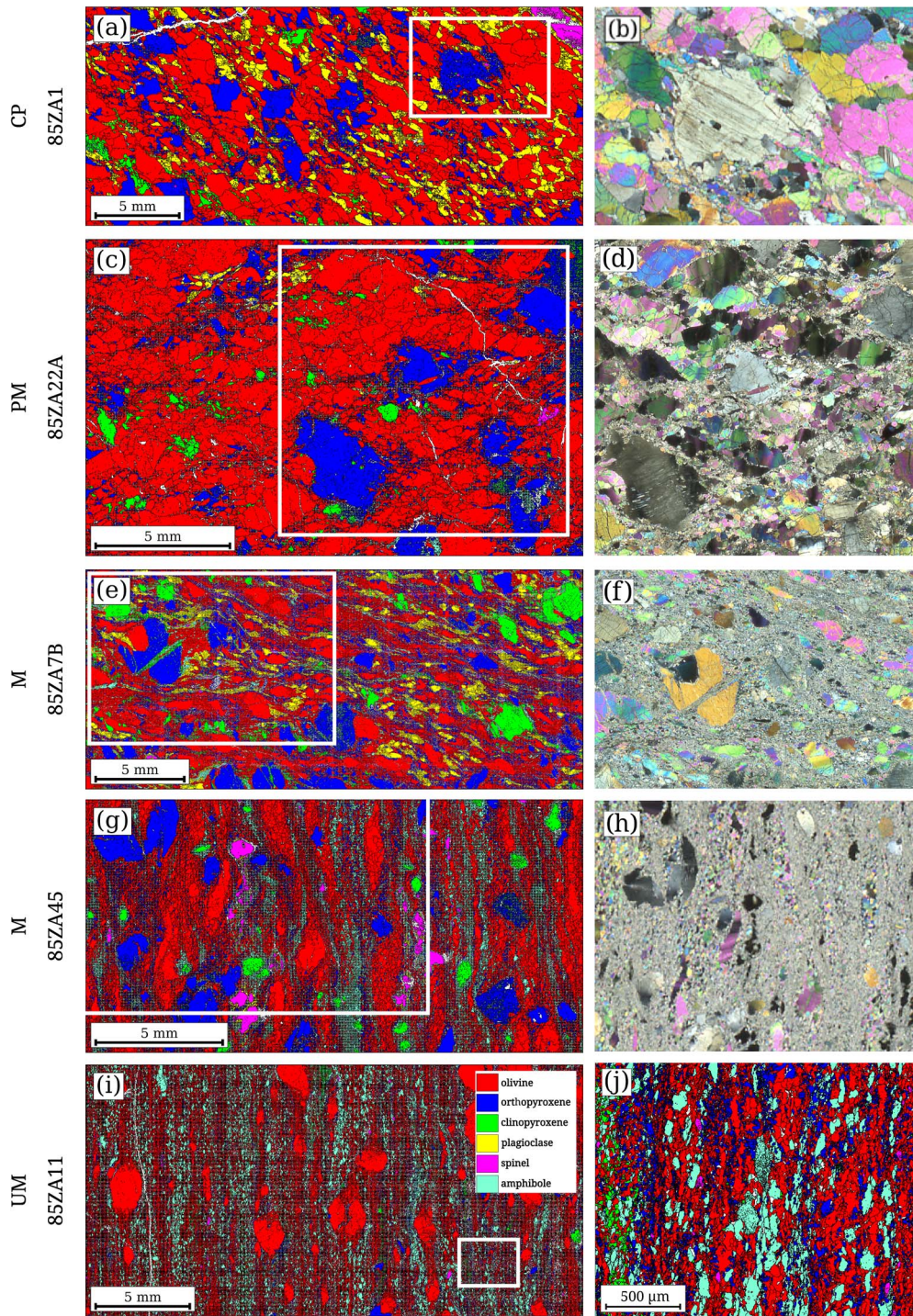


**Fig. 5.** Phase maps derived from (a, c, e, g, i, j) EBSD data and (b, d, f, h) photomicrographs illustrating typical (a, b) coarse-porphyroclastic, (c, d) protomylonitic, (e, f, g, h) mylonitic, and (i, j) ultramylonitic microstructures. White boxes in the left column panels define the location of the detail maps presented in the right column.

Fig. 6c) or troctolite (in the southern massif) at the mm to cm scale. Other samples have rather homogeneous compositions intermediate between that of a peridotite and a pyroxenite or a troctolite (Fig. 6e) at the thin section scale; they represent variations in modal composition occurring at the outcrop scale (tens of cm to meters) in the three massifs.

Amphibole is more common in the northern and central massifs. In all three massifs, amphibole-rich peridotites have dominantly mylonitic to ultramylonitic microstructures (Figs 2, 4, and 5g, i). Coarse-porphyroclastic peridotites have in

general low amphibole contents (Fig. 4; Table 1). High amphibole contents can be, nevertheless, observed locally, within a few mm or even cm of fractures, which crosscut the ductile foliation at variable angles in samples from all microstructural facies (Fig. 6e).

### Peridotites

Coarse-porphyroclastic peridotites are dominantly composed of coarse olivine, orthopyroxene, clinopyroxene, variable amounts of plagioclase (in the southern massif only), as well as minor spinel and amphibole (Figs 4, 5a, 6a–c). Olivine and orthopyroxene



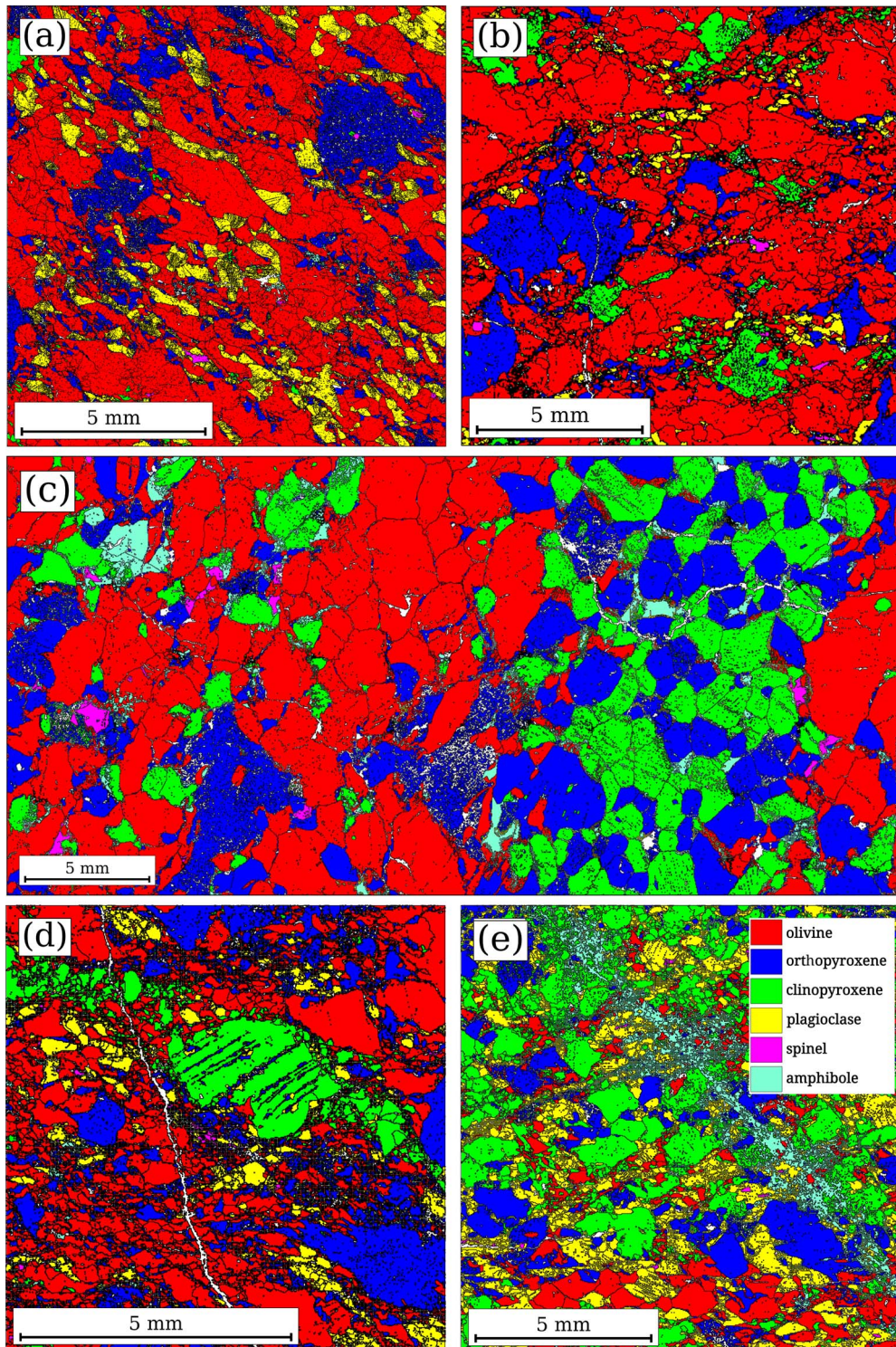


**Fig. 6.** Phase maps derived from EBSD data illustrating details of the (a) coarse-porphyroclastic microstructure in plagioclase-rich peridotite 85ZA1 from the southern massif, (b) coarse-porphyroclastic microstructure in clinopyroxene-rich peridotite 85ZA21 from the southern massif, (c) cm-scale pyroxenitic layer with diffuse limits parallel to the foliation marked by a weak shape preferred orientation of olivine in coarse-porphyroclastic spinel-peridotite 86Z30 from the central massif, (d) protomylonitic microstructure in plagioclase and clinopyroxene-rich peridotite 85ZA22b from the southern massif, and (e) coarse-porphyroclastic microstructure crosscut by a late amphibole-rich vein in sample 85ZA26C from the southern massif, which has troctolitic composition.

porphyroclasts are up to 5 mm long, but most often 1–2 mm (Figs 5a, b, 6a, b), while clinopyroxene and plagioclase are usually smaller than 2 mm. Coarse-porphyroclastic peridotites from the southern massif show a clear foliation and lineation marked by a shape-preferred orientation (SPO) of elongated olivine and pla-

gioclase grains (Figs 5a, 6a). Coarse-porphyroclastic peridotites from the central and northern massifs have a much weaker olivine SPO (more polygonal shapes and lower aspect ratios, Fig. 6c). They have, by consequence, a weaker foliation, but the latter is often underlined by spinel-websterite layers with diffuse



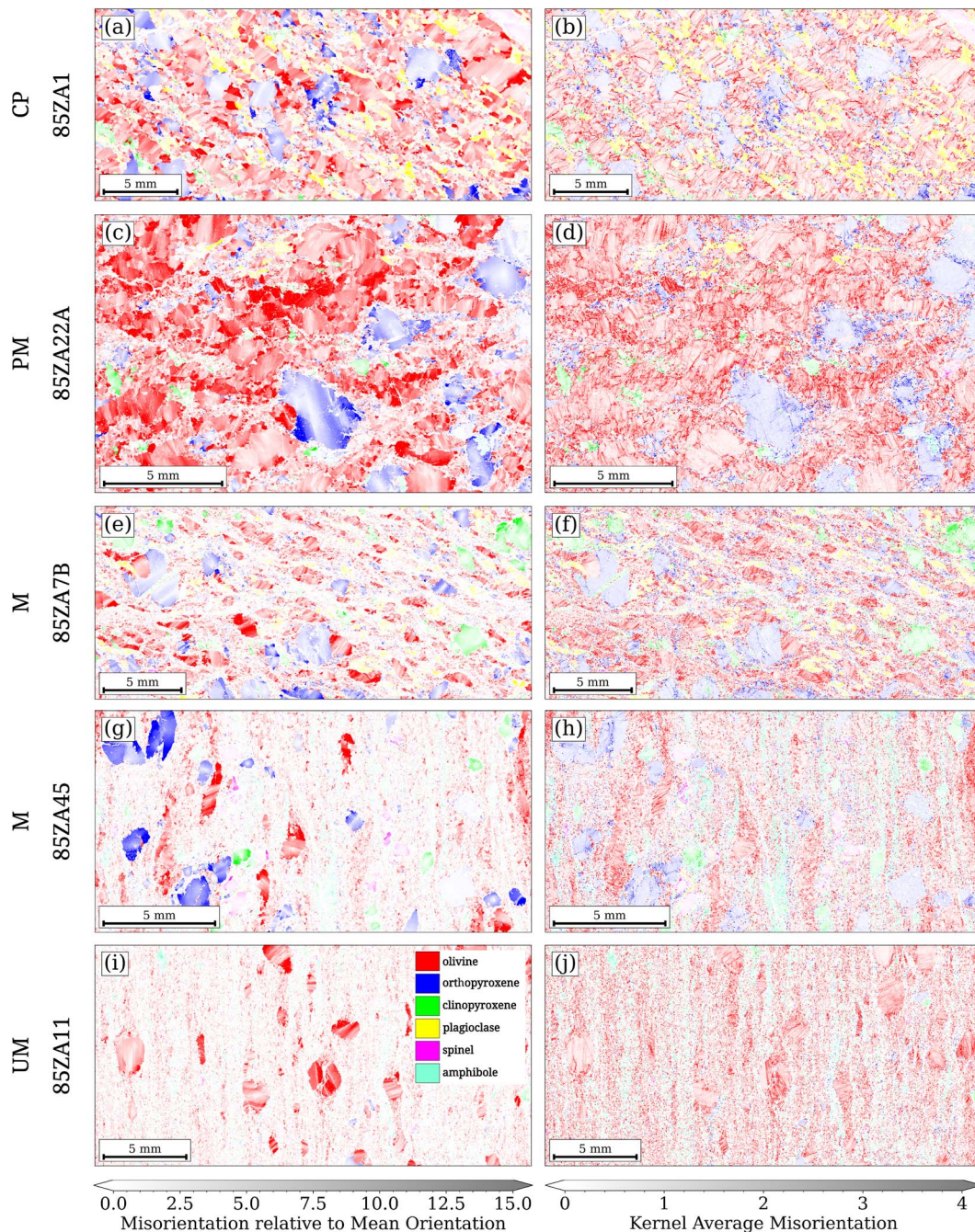


**Fig. 7.** (a, c, e, g, i) Misorientation relative to the mean orientation of the grain and (b, d, f, h, j) Kernel Average Misorientation (KAM) maps depicting the internal deformation of the grains in the different microstructural facies. High KAM values materialize subgrain boundaries. Grain boundaries are not displayed because they hinder the representation of the misorientation data in the small-sized neoblasts.

contacts with the peridotite (Fig. 6c). These websterite layers have thicknesses ranging from a few mm to tens of cm. Olivine-olivine grain boundaries are more sinuous in the southern massif (compare Fig. 6a-c). In coarse-porphyroclastic peridotites from all three massifs, olivine grains have well-developed sub-structures, characterized by widely spaced subgrain boundaries with strong misorientations at high angle to the grain elongation (Fig. 7a, b). Olivine grain sizes have a multimodal distribution (Fig. S2) and the neoblasts, which are on average coarser than 100  $\mu\text{m}$  (Fig. 3), are separated from the porphyroclasts mainly based on their lower intragranular misorientation.

In coarse-porphyroclastic peridotites of all three massifs, coarse orthopyroxene grains have variable sizes and irregular

shapes, often displaying embayments filled by olivine, and no SPO (Figs 5a, b and 6a-c). Coarse orthopyroxene grains often show undulose extinction (Figs 5b and 7a, b), but their intragranular misorientation is systematically lower than that of olivine. Smaller orthopyroxene grains have interstitial shapes with cusp-like terminations or film-like habitus along olivine-olivine grain boundaries (Figs 5a, b and 6a-c). Sometimes film-like orthopyroxene is in continuity with coarser grains. Clinopyroxenes have smaller sizes, but similar shapes to the orthopyroxenes (Figs 5a and 6b, c). In coarse-porphyroclastic peridotites from the southern massif, clinopyroxene grains tend to form trails parallel to the foliation (Fig. 5a). In coarse-porphyroclastic peridotites from the central and northern massifs, clinopyroxene is more



evenly distributed and both pyroxenes grain boundaries are less sinuous (Fig. 6c).

In coarse-porphyroclastic peridotites of the southern massif, plagioclase occurs mainly as elongated grains, 1 or 2 mm long, with interstitial shapes, but a well-defined SPO marking the foliation and lineation (Figs. 5a, 6a, b). Plagioclase also occurs in aggregates of smaller grains with rounded shapes rimming spinel. In coarse-porphyroclastic peridotites of the northern and central massifs, plagioclase is usually absent but may occur locally as tiny grains rimming spinel. Spinel occurs as coarse light-brown grains in association or not with pyroxenes. In the southern massif, spinel has irregular shapes that are elongated parallel to the lineation and is systematically rimmed by plagioclase aggregates (Figs. 5a, 6a, b). In coarse-porphyroclastic peridotites of the northern and central massifs, spinel has more rounded shapes and is usually associated with pyroxenes (Fig. 6c). Amphibole is always a minor phase in coarse-porphyroclastic peridotites. In the northern and central massifs, it occurs as mm-sized grains associated with clinopyroxene in the peridotites and as interstitial grains in the websterite layers (Fig. 6c). In the southern massif, amphibole may occur locally rimming plagioclase.

The protomylonites, which constitute the external domains of the shear zones, are characterized by the development of seams of a very fine-grained matrix forming a discontinuous anastomosed network at  $\pm 15^\circ$  on average to the elongation of the olivine porphyroclasts (Figs 5c, d and 6d). The fine-grained matrix is composed mainly of neoblasts of olivine with average grain sizes between 25 and 100  $\mu\text{m}$  (Fig. 3), but, locally, it also contains significant amounts of fine-grained orthopyroxene or clinopyroxene neoblasts (Fig. 6d). Olivine porphyroclasts are on average smaller and display more sinuous grain boundaries than in coarse-porphyroclastic peridotites (Figs 5c, d and 6d). They have a well-developed sub-structure, characterized by strong undulose extinction (Fig. 5d) and a high density of subgrain boundaries with strong misorientations at high angle to the grain elongation (Fig. 7c,d). As in coarse-porphyroclastic peridotites, orthopyroxene neoblasts have interstitial or film-like shapes, but they are significantly smaller (60–80  $\mu\text{m}$ , Fig. 3b) and tend to form asymmetric trails departing from the orthopyroxene porphyroclasts (Figs 5c and 6d). Clinopyroxene is smaller than orthopyroxene but has a similar habitus (Figs 5c and 6d). Plagioclase is on average smaller than in the coarse-porphyroclastic peridotites but displays a similar habitus (Figs 5c and 6d). In the more fertile samples, both clinopyroxene and plagioclase aggregates form trails that contribute in defining the foliation and lineation. Spinel occurs both as coarse grains rimmed by plagioclase and tiny grains dispersed in the matrix. Amphibole is rare, but may locally replace clinopyroxene and plagioclase in the fine-grained matrix network. In the present set of samples, most protomylonites come from the southern massif (Figs 1 and 3).

The mylonites are characterized by an increase in the fine-grained matrix fraction and a decrease in the size of the porphyroclasts (Figs 5e–h). The average size of the olivine neoblasts also tends to decrease but shows no clear correlation or anticorrelation with the olivine neoblast fraction (Fig. 3). The fine-grained matrix forms a continuous anastomosed network that encloses polycrystalline lenses up to 5 mm long, which preserve the microstructural record of the previous deformation steps (Figs 2, 5e–h, and 8a, c). The anastomosed matrix network together with the SPO of olivine porphyroclasts, as well as that of olivine and plagioclase aggregates, define a strong foliation and lineation (Figs 2, 5e–h, and 8a, c). The fine-grained matrix is

dominantly composed of intermixed olivine and orthopyroxene neoblasts with average grain sizes between 25 and 100  $\mu\text{m}$  (Fig. 3) but also contains neoblasts of other phases, in particular amphibole, in variable proportions (Figs 2, 5e, g and 8a, c). Olivine porphyroclasts are elongated, with a high density of subgrain boundaries normal to the elongation (Fig. 7e–h), and have well-developed core and mantle structures (Figs 2, 5e–h, and 8a, c). Clinopyroxene and plagioclase porphyroclasts display asymmetric trails of clinopyroxene and plagioclase neoblasts, respectively (Figs. 5e–h and 8a,c). Orthopyroxene neoblasts have interstitial, film-like shapes along olivine-olivine grain boundaries even far away from any orthopyroxene porphyroclast; these film-like orthopyroxenes are best developed along olivine grain boundaries at low angle to the foliation (Figs 2 and 8a, c). All phases, except amphibole, have a clear bimodal grain size distribution (Fig. S2). In mylonites from the southern massif, plagioclase usually shows a core and mantle structure (Fig. 8c) with a marked variation in composition. The cores of the porphyroclasts are more sodic than the rims and surrounding neoblasts (Fig. 8d). In mylonites of the northern and central massifs, plagioclase occurs as small grains rimming coarse spinels and as exsolutions in clinopyroxene (Fig. 8a). Spinel also occurs as small grains within the matrix with no plagioclase rims. Clinopyroxene and plagioclase are partially replaced by amphibole (Fig. 2); for a similar recrystallized fraction, the amount of amphibole tends to be higher in the mylonites of the northern and central massifs (cf. Figure 4). Some mylonites of the northern massif display two generations of amphibole, which differ in grain size and Ti content: the coarser amphiboles are enriched in Ti (Fig. 8b). One mylonite from the northern massif—85ZA51—has a particular microstructure: it is almost entirely composed of strongly recrystallized olivine (82%), amphibole (11%), and orthopyroxene neoblasts (6%), but neoblasts of olivine and amphibole are coarser grained than in the other mylonites.

The ultramylonites are characterized by almost total recrystallization. The fine-grained matrix occupies on average 60–70% of the thin section surface and  $\geq 50\%$  of the olivine fraction is composed of neoblasts. As in the mylonites, olivine neoblast grain sizes vary strongly among the samples and there is no clear correlation or anticorrelation between olivine neoblast grain sizes and area fraction (Fig. 3). The matrix is essentially composed of olivine, amphibole, and orthopyroxene neoblasts, with minor clinopyroxene and spinel, and traces of plagioclase (Figs. 5i, j). Most plagioclase as well as the majority of the clinopyroxene have been replaced by amphiboles. The strong foliation is underlined by variations in the olivine and amphibole contents, with local development of mm to cm wide amphibolite layers. The fine-grained matrix encloses rather coarse, millimetric to sub-millimetric olivine porphyroclasts with ellipsoidal shapes, which have a clear SPO, well-developed subgrain structures, and recrystallization tails (Figs 5i, j and 7i, j). Olivine porphyroclasts are locally rimmed or present fracture-like features filled by fine-grained orthopyroxene. Orthopyroxene porphyroclasts are rare.

A single ultramylonite sample—85ZA71-13—displays a microstructure indicating deformation at the brittle–ductile transition. This sample contains coarse olivine porphyroclasts crosscut by conjugated or extensional fractures sealed by either recrystallized olivine or a very fine-grained orthopyroxene matrix (Fig. 8e). These porphyroclasts are enclosed in a fine-grained matrix composed of olivine-, orthopyroxene-, amphibole-, or scapolite-rich layers or lenses. The mylonitic foliation defined by these almost monomineralic fine-grained layers is anharmonically folded (Fig. 8e). The amphibole-rich layers have a bimodal grain size, locally enclosing crystals hundreds of  $\mu\text{m}$

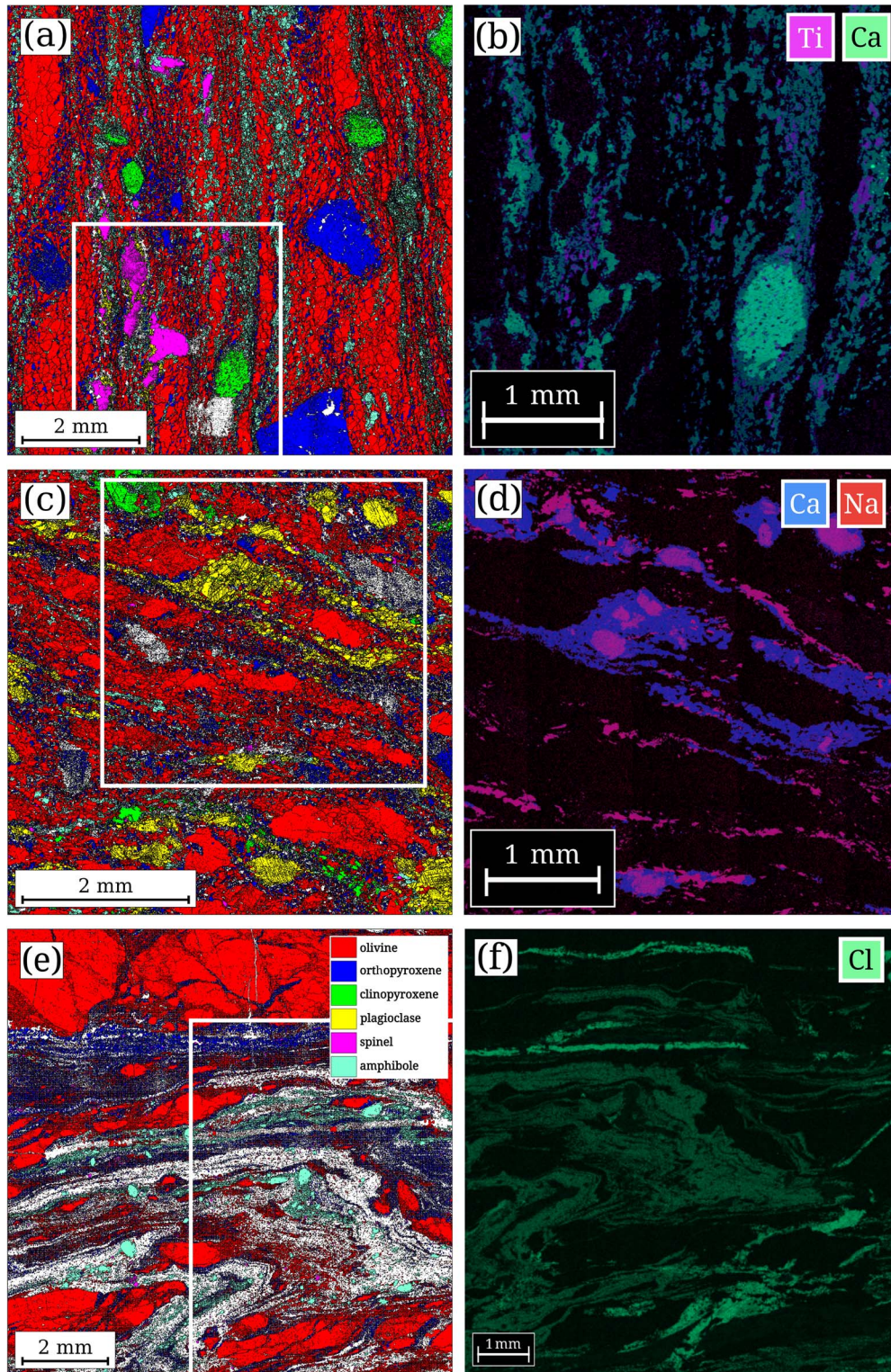


**Fig. 8.** (a, c, e) Phase maps derived from EBSD data and (b, d, f) compositional maps derived from EDS data illustrating microstructurally controlled variations in mineralogical composition in (a–d) mylonites and (e, f) ultramylonites. (b) Ti map documenting two generations of amphibole replacing clinopyroxene (green) in mylonite 85ZA45 of the northern massif: coarse amphiboles with high Ti contents (purple) are surrounded by finer-grained Ti-poor amphiboles (grey). (d) Ca + Na maps with magenta to blue tones documenting the increase in anorthite content in plagioclase from the core of porphyroclasts to the recrystallized grains in mylonite 95ZA7b of the southern massif. (e) Ultramylonite 85ZA71-13 from the southern massif displaying microstructures typical of the brittle-ductile transition; non-indexed (white) domains are scapolite-rich. This is corroborated by the Cl map in panel (f), where variations in cyan tones document the occurrence of two generations of scapolite with different Cl contents. White boxes in the left column panels define the location of the detail maps presented in the right column.



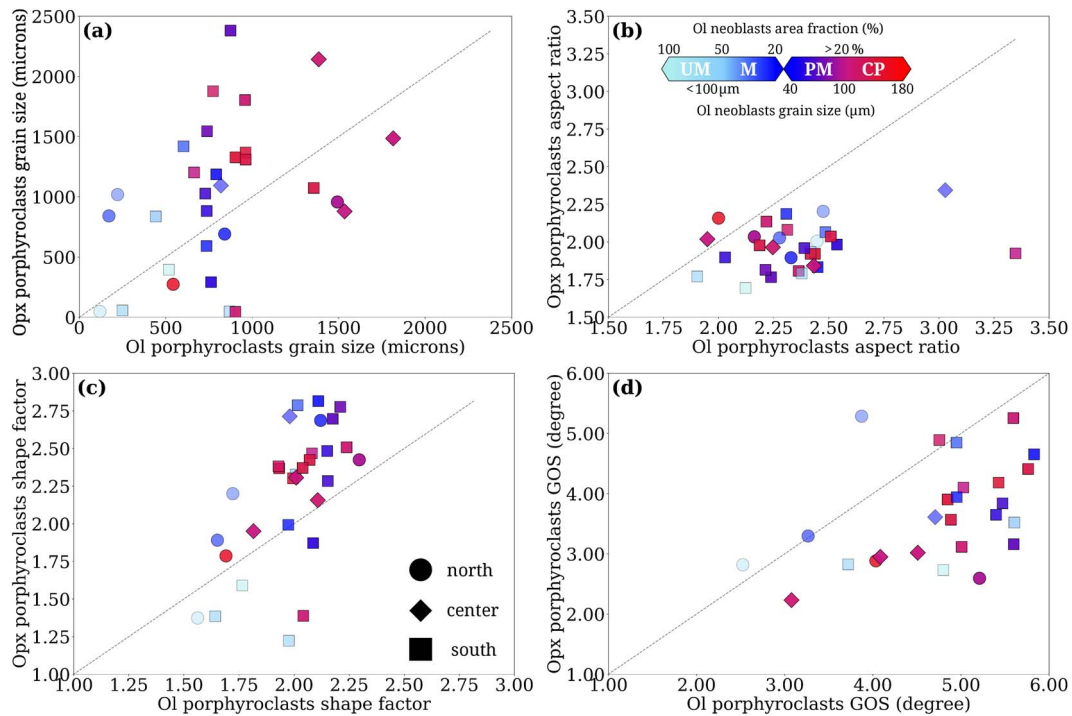


**Fig. 9.** Statistical microstructural data for olivine (Ol) and orthopyroxene (Opx) porphyroclasts: (a) grain size, defined by the equivalent grain diameter, (b) elongation, defined by the aspect ratio, (c) shape, defined by the shape factor, and (d) internal deformation, defined by the mean grain orientation spread (GOS). The values displayed are area-weighted averages over the entire EBSD map scale. This averaging was chosen to avoid over-representation of the numerous small grains that occupy in most cases a limited surface of the thin section. The dashed line marks the 1:1 relation.

wide (Fig. 8e). EDS analyses document two types of scapolite with variable Cl contents, which form independent layers (Fig. 8f). The Cl-rich scapolites are also S-rich. The scapolite-rich layers contain amphibole and plagioclase clasts. Biotite occurs locally within the fine-grained matrix, but chlorite is never observed.

### Websterites, wehrlites, and troctolites

In the central and northern massifs, pyroxenites are spinel websterites, which occur as diffuse layers of thicknesses ranging from a few mm to tens of cm. They have in general coarse-granular microstructures, being mainly composed of millimetric, equiaxed, but irregularly shaped, intermixed ortho- and clinopyroxene (Fig. 6c). These websterites also contain variable proportions of olivine with very irregular shapes, minor spinel, and up to 5% of amphibole, which occurs either replacing clinopyroxene or as isolated grains with interstitial shapes (Fig. 6c). Spinel grains are occasionally rimmed by plagioclase and amphibole. The peridotite in the vicinity of the websterite layers commonly displays film-like orthopyroxene grains along olivine-olivine grain boundaries (Fig. 6c).

In the central massif, at the contact with the gneisses, pyroxenite layers show ultramylonitic microstructures. All phases, except spinel, are largely recrystallized, forming a very fine-grained matrix (grain sizes  $\sim 25 \mu\text{m}$ ) that encloses rare orthopyroxene and clinopyroxene porphyroclasts. Ultramylonitic pyroxenites have higher plagioclase or amphibole contents than coarse-granular ones (cf. Fig. 4). Olivine and plagioclase are always fine-grained. Amphibole replaces clinopyroxene and to a lesser extent plagioclase and orthopyroxene.

Samples with wehrlitic to troctolitic compositions from the southern massif, like 85ZA26c or 85ZA71-12, display coarse granular to coarse porphyroclastic microstructures and a rough compositional layering, marked by variations in the olivine content

(Fig. 6e), parallel to the foliation of the associated peridotites. Plagioclase crystals have interstitial habitus. Coarse clinopyroxene crystals ( $>5 \text{ mm}$  in length) have thick exsolutions of orthopyroxene and plagioclase. Coarse orthopyroxene has finer clinopyroxene exsolutions. In the olivine-bearing layers, large polycrystalline lenses of plagioclase rim coarse spinel grains, with both the spinel grains and the plagioclase lenses elongated parallel to the lineation. In all three massifs, static replacement of clinopyroxene and plagioclase by amphibole is locally observed in the vicinity of straight millimetric-scale ultramylonite bands or healed fractures, which crosscut peridotites and pyroxenites with variable microstructures (Fig. 6e).

### Microstructure quantification

The evolution of the microstructure, illustrated above by representative examples, may be quantified for the entire dataset by the analysis of the area-weighted mean of the equivalent grain diameter, aspect ratio, shape factor, and mean intragranular misorientation of the olivine and orthopyroxene porphyroclasts (Fig. 9). We focused on the peridotites because the pyroxenites did not record the entire microstructural evolution. They are either not deformed under solid-state conditions (coarse granular microstructures) or ultramylonitic. We also based the analysis on the porphyroclasts, rather than the neoblasts, because the latter were often mapped by too few measurements ( $<10$  pixels) to have their shapes correctly described. Olivine and orthopyroxene were chosen because they are the dominant mineral phases in the peridotites. Moreover, as it will be discussed later, they represent end-members in terms of deformation processes: olivine microstructures result mainly from dislocation creep and dynamic recrystallization, whereas orthopyroxene microstructures result mainly from dissolution-precipitation, that is, interaction with a liquid phase (melt or aqueous fluid).

With rare exceptions, the olivine porphyroclasts average size decreases from millimetric in the coarse-porphyroclastic peridotites to  $<250\ \mu\text{m}$  in the ultramylonites (Fig. 9a). In contrast, the average size of the orthopyroxene porphyroclasts, which ranges from  $>2\ \text{mm}$  to  $<100\ \mu\text{m}$ , shows a large variation among the samples, but no systematic decrease from coarse-porphyroclastic peridotites to protomylonites. Orthopyroxene porphyroclasts sizes decrease, however, from the protomylonites to the mylonites and ultramylonites. In most samples, the orthopyroxene porphyroclasts are coarser than the olivine porphyroclasts. There are no systematic variations between peridotites from different massifs.

Comparison of the average aspect ratios of olivine and orthopyroxene porphyroclasts indicates that olivine is systematically more elongated than orthopyroxene (Fig. 9b). However, neither olivine nor orthopyroxene shows a systematic variation of the porphyroclast average aspect ratio between the different microstructures. Olivine in the coarse-porphyroclastic peridotites of the central and northern massifs tends to be less elongated than in the southern massif. Analysis of the phase maps of samples representative of the different microstructures (Fig. 5) shows that the elongated olivine porphyroclasts have a SPO, which materializes the lineation and foliation in all microstructural facies. In contrast, the orthopyroxenes, despite being anisometric, do not display a SPO consistent with the foliation and lineation. Orthopyroxenes usually have irregular shapes and, when they show a weak SPO, it is most often oblique to the foliation.

Orthopyroxene porphyroclasts have usually more sinuous grain boundaries than olivine porphyroclasts, quantified by their higher shape factor values (Fig. 9c). There is no systematic variation of the olivine porphyroclasts average shape factor between the different microstructures. There is no systematic variation of the sinuosity of orthopyroxene porphyroclasts grain boundaries between the coarse-porphyroclastic peridotites to the protomylonites but a clear decrease from the protomylonites to the ultramylonites.

The mean average intragranular misorientation, quantified by the GOS, is also, except for one mylonitic sample, systematically stronger in the olivine porphyroclasts than in the orthopyroxene porphyroclasts (Fig. 9d). There is no systematic variation of the GOS of the olivine and orthopyroxene porphyroclasts as a function of the microstructural facies.

## Crystal preferred orientations

Olivine crystal preferred orientations (CPOs) have dominantly orthorhombic symmetry (BA indexes between 0.35 and 0.65, Fig. 10a). Coarse-porphyroclastic peridotites have, nevertheless, a tendency towards axial-[010] patterns (BA-indexes  $<0.5$ , cf. red symbols in Fig. 10a). On average, the intensity of the olivine CPO (J index) decreases from the coarse-porphyroclastic peridotites to the ultramylonites. Separate analysis of the CPO of olivine porphyroclasts and neoblasts illustrates that the porphyroclasts CPO is systematically more concentrated (higher J indexes, Fig. 10b) than the neoblasts CPO in the same sample. It also shows that, with few exceptions, the neoblasts CPO has lower BA indexes than the porphyroclasts CPO, indicating that the process forming the neoblasts dispersed more the [100] axes than the [010] ones. Comparison of pole figures of the CPO of olivine porphyroclasts and neoblasts for a representative sample (85ZA1) illustrates this evolution (cf. inset in Fig. 10b). It also highlights the strong correlation between the porphyroclasts and neoblasts orientations, consistently with an inheritance of orientation during the formation of the neoblasts.

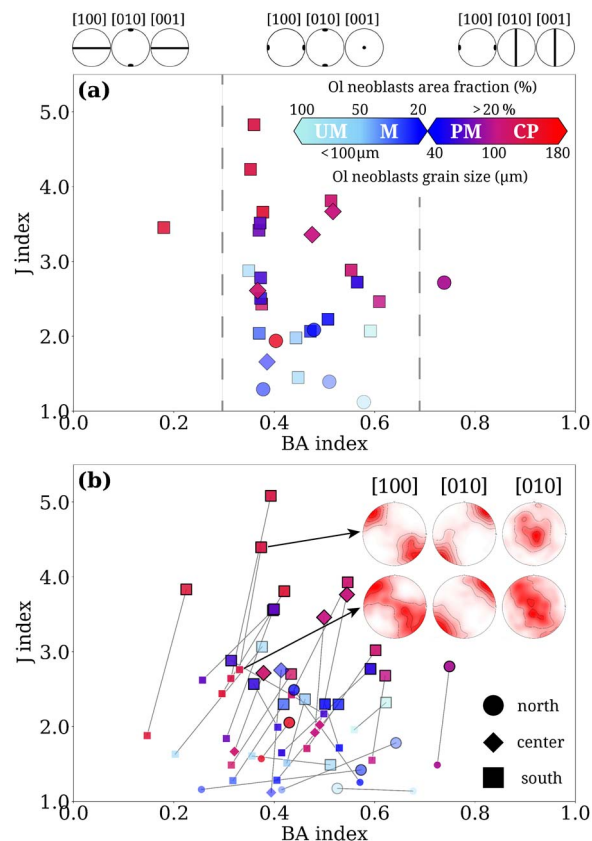


**Fig. 10.** Olivine crystal preferred orientation symmetry (quantified by the BA index) vs. intensity (quantified by J index). (a) Average values over the entire olivine population and (b) average values for porphyroclasts (coarse symbols) and neoblasts (small symbols); data for the same sample are linked by a line. Inset in (b) illustrates the difference in crystal preferred orientation of olivine between porphyroclasts and neoblasts (mean orientation of the grain) for a representative sample. Stereographic projections in the thin-section reference frame (cf. Fig. 5a); contours at one multiple of a uniform distribution interval.

Figure 11 illustrates the CPO of all major rock-forming minerals in the structural reference frame for representative samples of the different microstructural facies. Despite the decrease in intensity from coarse-porphyroclastic peridotites to ultramylonites, in all microstructural facies, the olivine CPO is characterized by a maximum of [100] aligned with the lineation and a maximum of [010] orthogonal to the foliation plane, with, in the rare samples that have an axial-[100] CPO, some dispersion of [010] in the YZ plane. In the coarse-porphyroclastic peridotites crosscut by cm-scale diffuse spinel-websterite (northern and central massif) or wehrlitic/troctolitic (southern massif) layers, the [010] maximum is normal to this layering. [001] is more dispersed. It may form a weak maximum normal to the lineation within the foliation, a rough girdle in the foliation plane, or a rough girdle normal to the lineation. Solely rare ultramylonites show a different olivine CPO, which is characterized by a double maxima, one parallel and the other normal to the lineation of either [100] (cf. sample 85ZA43B in Fig. 11a) or [001] (cf. samples 85ZA43B in Fig. 11a and 85ZA11 in Fig. 11b). Ultramylonite 85ZA71-13 has a complex olivine CPO due to folding of the mylonitic foliation (Fig. 11b).

Orthopyroxene CPO is highly variable (Fig. 11). In many samples, it is characterized by a maximum of [001] aligned with the lineation and the  $[100]_{\text{ol}}$  maximum and a maximum of [100] perpendicular to the foliation. However, very weak orthopyroxene CPO with secondary concentrations of [001] oblique to the

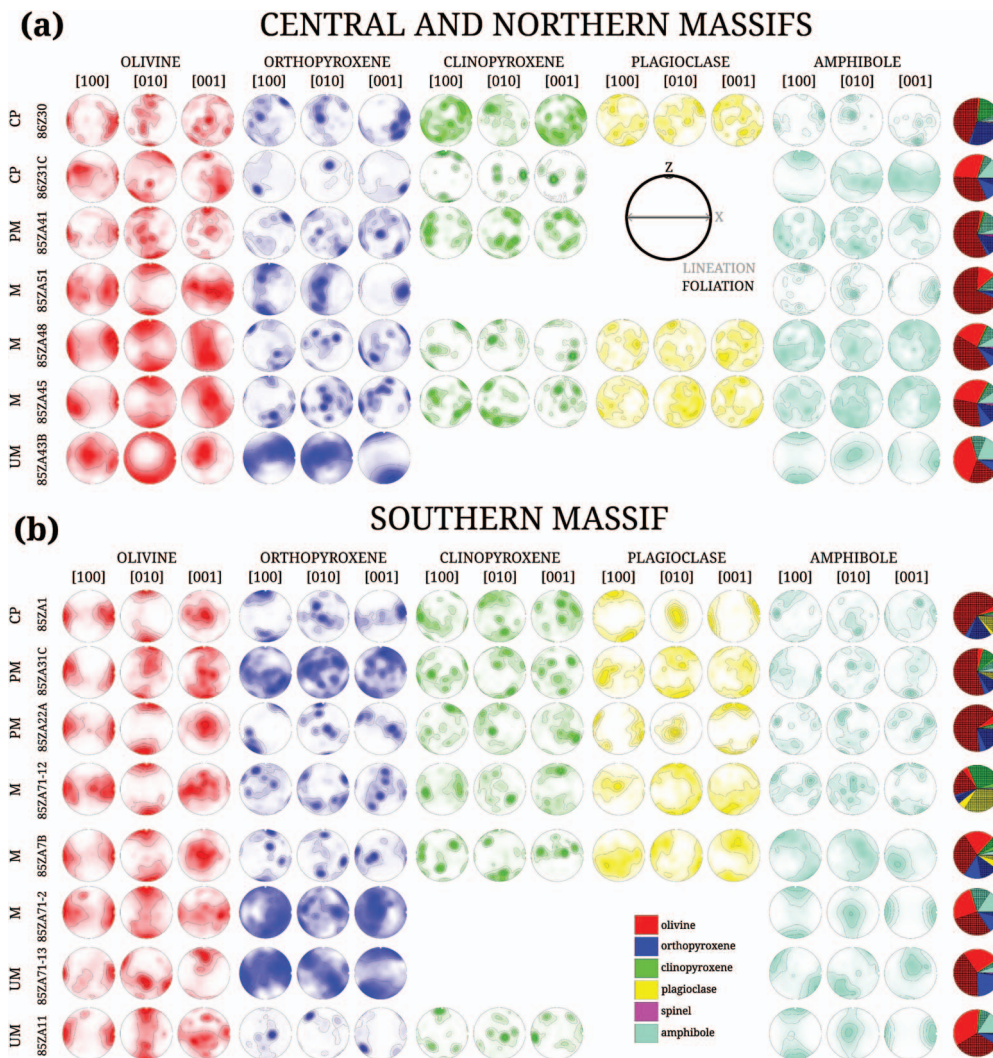


**Fig. 11.** Crystal preferred orientations of the main rock-forming minerals in samples representative of the different deformation facies in the (a) central and northern massifs and (b) southern massif. Contoured lower hemisphere stereographic projections in the structural reference frame (X is the lineation and Z is the normal to the foliation) of all measurements in the EBSD map. Contours at one multiple of a uniform density interval. Pie diagrams on the right show the modal composition of the samples with the hatched areas representing the porphyroclasts' area fraction for each mineral.

lineation is also common. In addition, some mylonites and ultramylonites show weak, but clear orthopyroxene CPO characterized by a maximum of [001] normal to the foliation (cf. samples 85ZA43B in Fig. 11a and 85ZA71-13 in Fig. 11b).

Clinopyroxene CPO is usually weaker than the olivine and orthopyroxene CPO (Fig. 11). Most coarse-porphyroclastic peridotites and protomylonites display, nevertheless, some alignment of [001] parallel to the lineation. In the mylonites and ultramylonites, the clinopyroxene CPO is poorly defined, with multiple maxima due to the presence of a few porphyroclasts. In some samples, one of the [001]<sub>cpx</sub> maxima is aligned with the lineation and the [100]<sub>ol</sub> maximum, but in most cases, there is no clear relation between the clinopyroxene CPO and the structural reference frame. Clinopyroxene in the websterite layers that crosscut the coarse-porphyroclastic peridotites in the central and northern massif shows a girdle distribution of [001]<sub>cpx</sub> in the layering plane. In contrast, clinopyroxene in the troctolitic layers in the southern massif shows a concentration of [001]<sub>cpx</sub> at high angle to the layering.

In coarse-porphyroclastic peridotites and protomylonites, the plagioclase CPO is characterized by either a [001] maximum

slightly oblique to the lineation and a (100) maximum parallel to the foliation or the opposite (Fig. 11). In the mylonites, plagioclase CPO are weaker and characterized by a poor alignment of the normal of (010) with the lineation and of [100] normal to the foliation. The plagioclase fraction in the mylonites of the northern and central massifs and in the ultramylonites, in general, is too low for a quantitative analysis of the CPO.

In coarse-porphyroclastic peridotites and protomylonites, the amphibole content is often low and its CPO is not clearly defined, displaying multiple maxima. It often mimics the cpx CPO (Fig. 11). In mylonites containing significant amounts of amphibole, the amphibole CPO, which is most often weak, is characterized by a [001] maximum at a low angle or parallel the lineation and the [100]<sub>ol</sub> maximum and concentration of (100) at a low angle to the foliation. However, in some mylonites, amphibole has a CPO characterized by a girdle distribution of [001] in the XZ structural plane, which mimics, although more dispersed, the clinopyroxene CPO (Fig. 11). In amphibole-rich ultramylonites, amphibole displays a strong CPO characterized by alignment of [001] with the lineation and the [100]<sub>ol</sub> maximum and of (100) with the foliation (Fig. 11).



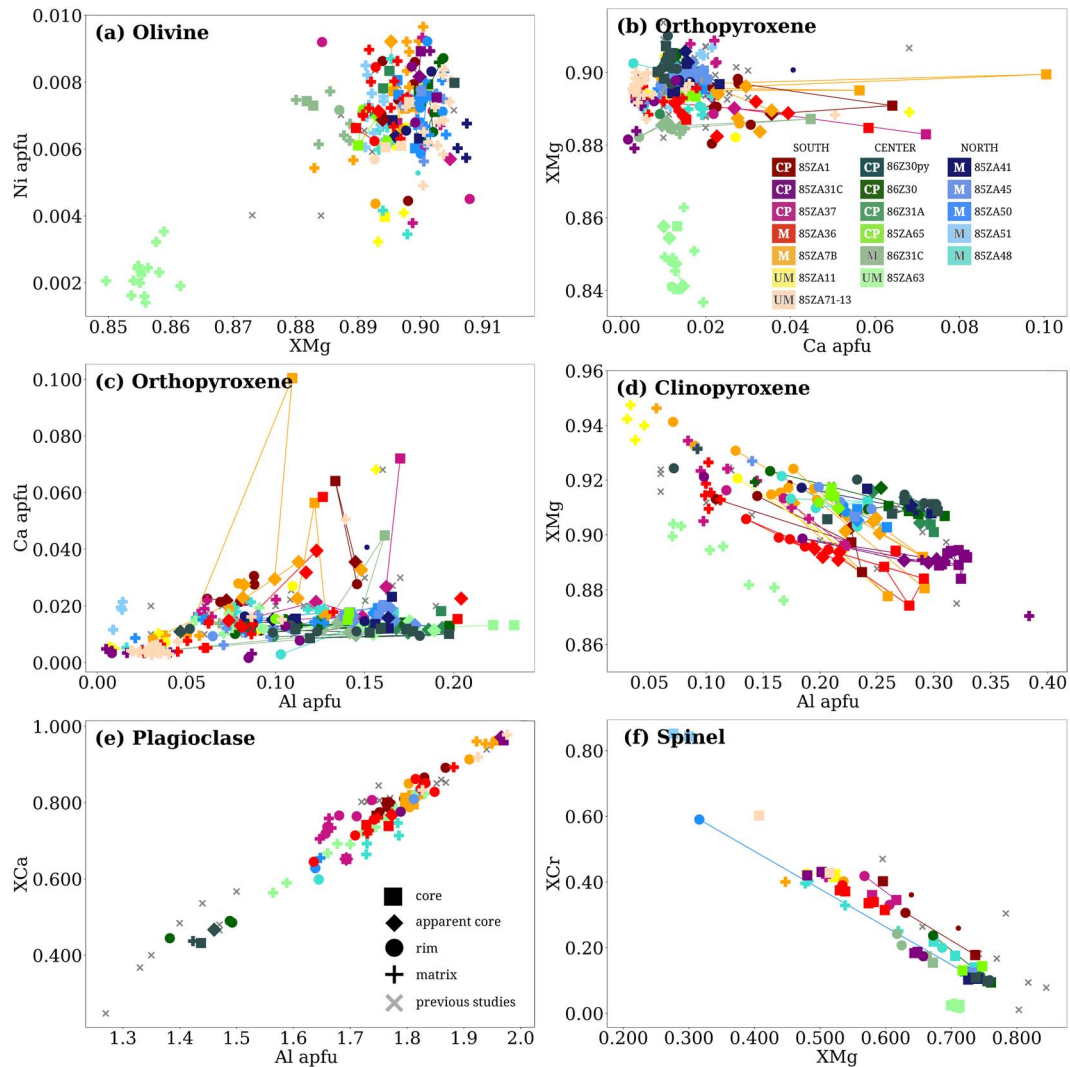


**Fig. 12.** Compositions of olivine, orthopyroxene, clinopyroxene, plagioclase, and spinel in atoms per unit formula. Symbols indicate the type of analysis: core, intermediate, or rims of porphyroclasts, or neoblasts within the fine-grained matrix. Lines linking core, intermediate, and rim symbols indicate data collected in a single grain. Warm colours indicate samples from the southern massif, greens, samples from the central massif and blues, samples from the northern massif. Lighter tones indicate more recrystallized samples.

## Mineral chemistry

Olivine has  $X_{Mg}$  ( $Mg/(Mg + Fe)$  apfu, atoms per formula unit) varying from 0.88 to 0.91 and Ni contents ranging from 0.0035 to 0.01 apfu in the peridotites and cm-scale websterite layers (Fig. 12a). Olivine in the thicker pyroxenite 85ZA63 has significantly lower  $X_{Mg}$  (0.85–0.86) and Ni content (0.0017–0.004 apfu). Compositions, in particular Ni contents, are highly variable both among samples and within each sample, but no systematic variation between core, rims, or neoblasts within a sample or correlation with neither the microstructural facies of the sample nor the provenance (massif) are observed. The variability in olivine compositions documented in the present study is consistent with previous data by Bonatti *et al.* (1986) and Piccardo *et al.* (1988).

Orthopyroxene is enstatite with  $X_{Mg}$  ranging between 0.88 and 0.91 in the peridotites and cm-scale pyroxenite layers in the composite samples and between 0.83 and 0.87 in the websterite 85ZA63 (Fig. 12b). As for olivine, there are no systematic variations in  $X_{Mg}$  of orthopyroxene as a function of the microstructure or provenance. In contrast, Ca contents systematically decrease from core to rim in the porphyroclasts and to the neoblasts within most samples (Fig. 12b). An exception is pyroxenite

85ZA63, where orthopyroxene has rather homogeneous low Ca contents, that are slightly higher in some neoblasts. Another exception is an orthopyroxene neoblast in an amphibole-rich domain in ultramylonite 85ZA11, which displays a high Ca content ( $>0.06$  apfu), whereas most orthopyroxenes in this sample have Ca contents  $<0.01$  apfu. Ca content in orthopyroxene also varies systematically with provenance: the highest Ca contents ( $>0.06$  apfu) were measured in the cores of orthopyroxene porphyroclasts of peridotites from the southern massif. Aluminium contents in orthopyroxene are also highly variable (from 0.005 to 0.30 apfu) and decrease rather systematically from core to rim in the porphyroclasts and to the neoblasts, except for two neoblasts in ultramylonite 85ZA11 that have high Al contents (Fig. 12c). In contrast to the Ca contents, the highest Al contents and most marked decrease in Al content from core to rim in the porphyroclasts and to the neoblasts were measured in peridotites and pyroxenites of the central and northern massifs.

Clinopyroxene is diopside with  $X_{Mg}$  ranging between 0.88 and 0.95. The Al content, which varies from 0.05 to 0.30 apfu, is anticorrelated with  $X_{Mg}$ , defining three trends: (1) a flatter trend for the peridotites of the central and northern massif, (2) a steeper



trend for the peridotites of the southern massif, and (3) a similarly steep trend but at low  $X_{Mg}$  values for the intergranular variability in the fine-grained matrix of websterite 85ZA63 (Fig. 12d). In the peridotites, these trends record a systematic increase in  $X_{Mg}$  and a decrease in Al content from core to rim in the porphyroclasts and even more in the neoblasts within the individual samples. The decrease in  $X_{Mg}$  is more marked in the peridotites of the southern massif. There is no systematic variation of Cr and Ti contents in clinopyroxene with the sample provenance or microstructure; most samples have Cr contents in clinopyroxene between 0.15 and 0.04 apfu and Ti contents below 0.025 apfu (Supporting Information Table S2). However, in most samples, the Cr content in clinopyroxene decreases from core to rim in the porphyroclasts and even more in the neoblasts (Supporting Information Table S2). The present analyses are consistent with previous data by Bonatti *et al.* (1986) and Piccardo *et al.* (1988), including the contrast in clinopyroxene compositions between the southern massif and the central and northern massifs.

Plagioclase displays an extreme variation in Al content and  $X_{Ca}$  ( $Ca/(Ca + Na)$  apfu) from andesine to anorthite ( $X_{Ca}$  0.4 to >0.9, Fig. 12e). Plagioclase in peridotitic and websteritic layers of protomylonite 86Z30 from the central massif is andesine ( $X_{Ca}$  of 0.4–0.5). Labradoritic compositions ( $X_{Ca}$  0.5–0.7) are observed in plagioclases rimming spinel in mylonites and ultramylonites in the central and northern massifs (85ZA63, 85ZA50, and 85ZA48) as well as in the coarse-porphyroclastic peridotite 85ZA37 and mylonite 85ZA36 from the southern massif. The cores and rims of plagioclase porphyroclasts in coarse porphyroclastic peridotites 85ZA1 and 85ZA37 and mylonites 85ZA36 and 85ZA7b from the southern massif, as well as some neoblasts in mylonites of the central and northern massifs, are bytownite ( $X_{Ca}$  0.7–0.9). Finally, the rims and matrix grains of mylonite 85ZA7b and ultramylonite 85ZA71–13 and some coarse grains in the troctolitic layer in protomylonite 85ZA31c from the southern massif have anorthitic compositions ( $X_{Ca}$  > 0.9). On average, plagioclases in the central and northern massifs have lower Ca and Al contents than in the southern massif (Fig. 12e). At the sample scale, both coarse porphyroclastic peridotite 85ZA1 and mylonite 85ZA7b show enrichment in  $X_{Ca}$  from core to rim of the porphyroclasts and to the neoblasts (Fig. 12e), which had also been documented by EDS mapping (Fig. 8d). The present analyses are consistent with previous data by Bonatti *et al.* (1986) and Piccardo *et al.* (1988), but some plagioclases analysed by Piccardo *et al.* (1988) display significantly lower Ca contents (Fig. 12e).

Spinel displays extreme variations in both  $X_{Mg}$  and  $X_{Cr}$  ( $Cr/(Cr + Al + Fe^{3+})$  apfu) (Fig. 12f). Spinel in coarse porphyroclastic and protomylonitic peridotites and coarse-granular websterite layers in the northern and central massifs display the highest  $X_{Mg}$  (~0.75) and the lowest  $X_{Cr}$  (~0.1; Fig. 12f). The lowest  $X_{Mg}$  (~0.25) and highest  $X_{Cr}$  (~0.9) are displayed by ultramylonite 85ZA51 from the northern massif. Peridotites from the southern massif show intermediate values, but also present a trend of decrease in  $X_{Mg}$  and increase in  $X_{Cr}$  with increasing localized deformation. In addition, all samples show enrichment from cores to rims to matrix in Cr and Fe. The most extreme variation ( $X_{Cr}$  0.1–0.6,  $X_{Mg}$  0.7–0.2) is displayed by mylonite 85ZA50 from the northern massif. Relative to the peridotites, spinels in the websterite 85ZA63 are enriched in Al for a given  $X_{Mg}$ . The present analyses are consistent with those from Bonatti *et al.* (1986), but we sampled a higher variability in spinel composition. Some spinels analysed by Piccardo *et al.* (1988) have higher  $X_{Mg}$ .

As observed in previous studies (Bonatti *et al.*, 1986; Piccardo *et al.*, 1988; Agrinier *et al.*, 1993), amphiboles have a wide range

of compositions, from Ti-rich pargasite to tremolite (Fig. 13a, b), based on structural formulae calculated following Li *et al.* (2020). Pargasite with <0.2 apfu Ti occurs in coarse-porphyroclastic peridotites from the three massifs (Fig. 13b). Synkinematic amphiboles in mylonites of the three massifs are also dominantly pargasite, but with lower Ti contents, or magnesio-hornblende. In ultramylonites, amphibole compositions range from Ti-poor pargasite to magnesio-hornblende, marking a trend of decreasing Ti,  $Al^{IV}$  and Na + K contents with increasing low-temperature deformation (Fig. 13a, b). The lowest  $Al^{IV}$  and Na + K contents are observed in a matrix amphibole of mylonite 85ZA50 and in amphiboles that statically replace clinopyroxenes in the vicinity of a fracture in protomylonites 85ZA41 and 85ZA31c. Note that static amphiboles in these two samples show a wide range of compositions covering most of the  $Al^{IV}$  vs. Na + K trend of the Zabargad data (Fig. 13a), but they have systematically low Ti and high Si contents (Fig. 13b). The two petrographically distinct generations of amphibole in mylonites 85ZA48 and 85ZA45 (cf. Fig. 8b) display a consistent variation in Ti (Fig. 13b) and Na + K contents (Fig. 13a). Synkinematic amphiboles from mylonite 85ZA51 are slightly offset from the major trend, being enriched in Na + K relative to their  $Al^{IV}$  content (Fig. 13a). These amphiboles are enriched in Cr (0.35–0.4 apfu) relative to the main Zabargad amphibole population (Fig. 13c). A similar offset is displayed by some analyses of amphiboles of the northern massif by Agrinier *et al.* (1993) and to a lesser extent by Bonatti *et al.* (1986) and Piccardo *et al.* (1988). Amphiboles from ultramylonitic websterite 85ZA63, which were also previously analysed by Agrinier *et al.* (1993), have highly variable compositions (Fig. 13a–c).

Amphiboles in coarse-porphyroclastic peridotites 86Z30 and 86Z31a from the central massif and 85ZA37 from the southern massif have very low Cl contents, but coarse-porphyroclastic peridotite 85ZA1 from the southern massif has Ti-rich pargasite rimming plagioclase with Cl contents up to 0.08 apfu (Fig. 13d). In the southern massif, the Cl content in amphibole attains >0.13 apfu in mylonite 85ZA7b and decreases to 0.05–0.10 apfu in ultramylonites 85ZA11 and 85ZA71–13. Mylonites from the northern and central massifs display highly variable Cl contents, covering the entire range of observations, and no simple relation between the Cl and Si content (Fig. 13d). Cl contents in amphiboles that statically replace clinopyroxene in the vicinity of fractures are low and independent of the Si content in protomylonite 85ZA41 but high and anti-correlated with the Si content in protomylonite 85ZA31C (Fig. 13d).

## Equilibrium pressures and temperatures

Equilibrium temperatures have been estimated using the Al–Cr and the Ca in orthopyroxene thermometers (Figs. 14a, b). Both thermometers predict a decrease in equilibrium temperature from core to rim in the porphyroclasts and then to the matrix within individual samples. They also predict a consistent decrease in equilibrium temperature with increasing localized deformation within the entire dataset, with the highest temperatures predicted for the cores of orthopyroxene porphyroclasts in the coarse-porphyroclastic peridotites and the lowest temperatures for orthopyroxene neoblasts in the matrix of ultramylonites. However, the plot of the Al content in orthopyroxene versus the temperatures estimated using the Al–Cr in orthopyroxene thermometer shows distinct trends for the southern or central and northern massifs (Fig. 14a). For comparable Al contents, lower equilibrium temperatures are predicted for the central and northern massifs. This highlights a possible effect of pressure on this system. In contrast, temperatures

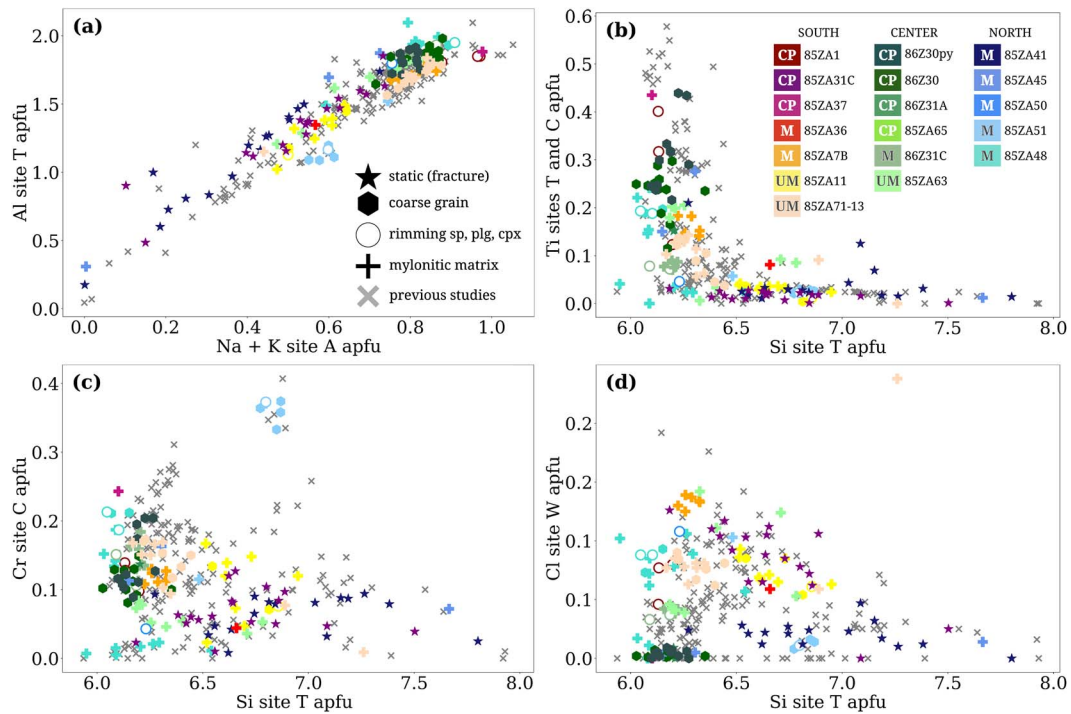


**Fig. 13.** Compositions of amphiboles in atoms per unit formula (assuming a general formula  $A_{0-1}B_2C_5T_8O_{22}W_2$ ). Symbols indicate the type of analysis: coarse or fine grains in the mylonitic matrix, rims around spinel, clinopyroxene, or plagioclase, or crystals formed by static replacement of clinopyroxene (mostly) in the vicinity of fractures. Warm colors indicate samples from the southern massif, greens, from the central massif, and blues, from the northern massif. Lighter tones indicate more recrystallized samples.

predicted using the Ca in orthopyroxene thermometer versus Ca contents neatly materialize the exponential relation used to adjust the experimental data for the thermometer, indicating a lower pressure sensitivity (Fig. 14b). Note, however, that the lowest temperatures predicted by this thermometer (as low as 550°C, Fig. 14d) are inconsistent with the absence of chlorite in these rocks, which should be stable in a hydrated fertile ultramafic system below ca. 700°C (cf. thermodynamic modelling section below).

Equilibrium pressures may be estimated based on the plagioclase and pyroxenes compositions (Borghini *et al.*, 2010; Fumagalli *et al.*, 2017). The present data correlate well with Fumagalli *et al.* (2017) data for fertile compositions, which showed an increase  $Al^{IV}$  in clinopyroxene (from 0.06 to 0.16) and a decrease in  $X_{Ca}$  of plagioclase (from 0.83 to 0.50) with increasing pressure from 0.3 to 0.9 GPa. Within each sample, despite the strong dispersion in the measurements, the median  $Al^{IV}$  in clinopyroxene decreases from core to rims in the porphyroclasts, and further in the matrix grains (Fig. 14c). In most peridotites from the northern and central massifs and in coarse-porphyroclastic peridotite 85ZA37 from the southern massif, the  $Al^{IV}$  in clinopyroxene displays a rough negative correlation to the  $X_{Ca}$  of plagioclase (Fig. 14c). The lowest  $X_{Ca}$  and the highest  $Al^{IV}$  contents were measured in the cores of plagioclase and clinopyroxene porphyroclasts, respectively, from coarse-porphyroclastic peridotites and associated websterite layers from the central massif. The highest  $X_{Ca}$  is displayed by plagioclase in the matrix of mylonite 85ZA7b. It is noteworthy that the cores of plagioclase and clinopyroxene porphyroclasts in coarse-porphyroclastic peridotite 85ZA36 from the southern massif have compositions similar to those of plagioclase and clinopyroxene rims in mylonite 85ZA50 from the northern massif (Fig. 14c). In coarse-porphyroclastic peridotites 85ZA1, 85ZA37, 85ZA31c, and mylonite 85ZA7b of the southern massif as well as

mylonite 85ZA45 of the northern massif, the  $Al^{IV}$  in clinopyroxene varies strongly at roughly constant  $X_{Ca}$  of plagioclase (Fig. 14c). The present results are consistent with previous data by Bonatti *et al.* (1986) and Piccardo *et al.* (1988), including the contrasting compositions between the southern massif and the central/northern ones.

The pressures calculated using the FACE barometer of Fumagalli *et al.* (2017) based on the temperature estimates with the Ca in orthopyroxene thermometer imply a progressive decrease in equilibration pressure in all three massifs (Fig. 14d). This evolution is consistent with the enrichment in Ca in the plagioclase rims and the neoblasts relative to the cores of the porphyroclasts observed in the mylonites of the southern massif (Fig. 8d) and with similar inverse anorthite-zoning described in lherzolites recrystallized at plagioclase facies conditions during progressive exhumation in the Horoman and Liguride ophiolites (Ozawa & Takahashi, 1995; Borghini *et al.*, 2010).

In the southern massif, we document both cooling and decompression associated with the localized deformation. The composition of the cores in coarse-porphyroclastic, protomylonitic, and mylonitic peridotites, as well as previous data by Bonatti *et al.* (1986), points to initial pressures >0.7 GPa and temperatures ~1200°C, which evolve during the localized deformation to 900–800°C and 0.5–0.3 GPa based on rim and matrix neoblasts data. Intermediate pressures and temperatures (<1000°C at ~0.6 GPa) are recorded by the compositions of partially re-equilibrated cores. The matrix data of mylonite 85ZA7b results in equilibration temperatures ~700°C, but negative pressures, indicating re-equilibration outside the conditions used in the calibration of the FACE barometer.

In the central and northern massifs, the thermobarometric data for both peridotites and websterites point to almost isothermal decompression at 750–850°C, starting at >0.8 GPa (core

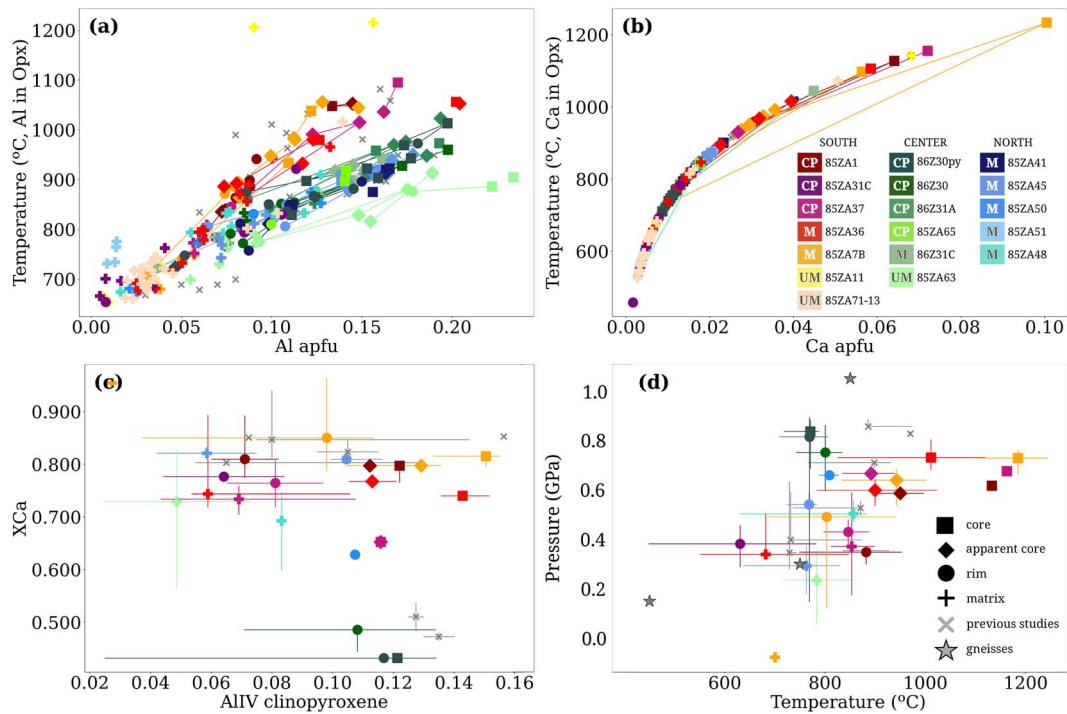


**Fig. 14.** Equilibrium temperature and pressure conditions estimated for the different microstructural assemblages in each sample: cores, apparent cores, and rims of porphyroclasts or neoblasts from the recrystallized matrix. (a) Al in orthopyroxene (in atoms per formula unit, apfu) vs temperatures estimated using the Al in orthopyroxene thermometer, the difference in temperature estimates for similar Al contents between samples from the central and northern massifs and the southern massif denote the effect of pressure on this thermometer. (b) Ca content in orthopyroxene (apfu) vs temperatures estimated using Ca in orthopyroxene thermometer. (c) Al<sup>IV</sup> in clinopyroxene versus X<sub>Ca</sub> in plagioclase. (d) Ca in orthopyroxene temperatures vs pressures estimated using the FACE barometer for all plagioclase-bearing microstructural assemblages. In (a) and (b) results of individual analyses are presented (error bars are smaller than the symbols). In (c) and (d) the uncertainty due to spatial variations in the minerals composition within a sample was estimated by considering all possible combinations between cores, apparent cores, rim, and matrix analyses for the different minerals in each sample; it is represented by plotting the median with error bars representing the dispersion of the estimated values for each microstructural class.

and rim data in coarse porphyroclastic peridotite 86ZA30) and ending at ~0.2 GPa (matrix data in mylonites 85ZA45 and 85ZA63). Higher temperatures (>900°C) at ~0.8 GPa are predicted based on previous analyses by Bonatti *et al.* (1986) and Piccardo *et al.* (1988). This evolution is consistent with previous estimates by Piccardo *et al.* (1988) based on the Ca-Tschermak and enstatite contents in clinopyroxene from peridotites and pyroxenites of Zabargad. It is also consistent with the equilibration conditions inferred for the gneisses co-deformed at the contact with mylonitic peridotites of the central massif (Fig. 14d), which evolved from 850 to 800°C at 1.05 GPa to 700–800°C at 0.3 GPa (Boudier *et al.*, 1988; Seyler & Bonatti, 1988). In these gneisses, analysis of fluid inclusions suggests additional exhumation and cooling to pressures up to 0.15 GPa and temperatures of 450°C (Boullier *et al.*, 1997).

## DISCUSSION

### Evolution of deformation conditions and deformation processes

The present petrostructural data document the evolution of deformation processes and reactions during the exhumation of the mantle along extensional shear zones during the formation of the Red Sea rift. In the three peridotite massifs, strain localization into progressively smaller volumes (discrete shear zones) preserved a complete record of the evolution of deformation at decreasing temperature and pressure conditions. The last stages of deformation recorded in all three massifs correspond to very shallow depths (<0.3 GPa), but still elevated temperatures (>700°C,

constrained by the absence of chlorite). However, the petrostructural record in the southern and central/northern massifs implies markedly different initial conditions. The pervasive deformation recorded in the southern massif occurred in a shallow (< 30 km depth) lithosphere–asthenosphere boundary, whereas the pervasive deformation in the central and northern massifs is associated with thinning of a deep section of the subcontinental lithospheric mantle, which probably still had a ≥ 30 km thick continental crust attached to it. Despite this difference in initial conditions, the active deformation processes and the role of melts and fluids in the different stages of mantle exhumation are similar.

### Pervasive deformation—coarse-porphyroclastic microstructures

Analysis of the microstructures and CPO of the coarse-porphyroclastic peridotites indicate that the pervasive deformation in the three massifs occurred by melt-assisted dislocation creep under near solidus conditions. The coarse-porphyroclastic peridotites have a clear foliation and lineation materialized by the shape preferred-orientation of elongated olivine crystals with strong intragranular deformation (subgrains and undulose extinction, cf. Figures 5a, b, 6a, b, 7a, b, and 8b, d) and CPO (Figs. 10 and 11). Thus, olivine, which is the volumetrically dominant phase, forming a continuous stress-bearing framework in peridotites, deforms essentially by dislocation creep. However, coarse-porphyroclastic peridotites also display widespread evidence of deformation in the presence of melts. The parallelism between the diffuse websteritic (in the central/northern massifs) or

troctolitic (in the southern massif) layering and the foliation marked by the olivine elongation (Fig. 6c, e) indicates that the reactive melt percolation producing this layering is synkinematic, with the deformation controlling the melt distribution (e.g. Holtzman et al., 2003a; Higgie & Tommasi, 2012, 2014; Frets et al., 2014; Tommasi et al., 2017). Reactive melt percolation is further documented in the peridotites by the irregular shapes of coarse orthopyroxene crystals as well as cusp-shaped terminations and film-like habitus of orthopyroxene neoblasts along olivine grain boundaries (Figs 5a, b and 6a–c), which record dissolution and precipitation from a liquid phase, respectively. The film-like orthopyroxene crystals are best developed along olivine grain boundaries at low angle to the foliation, indicating a structural control on their formation. The preservation of such grain shapes implies, nevertheless, limited deformation subsequent to their crystallization. In addition, peridotites from the southern massif have high contents of plagioclase (Figs 4 and 5a), which cannot result from subsolidus re-equilibration of spinel peridotites. The interstitial, but elongated shape of the plagioclase and clinopyroxene in these peridotites, together with a CPO consistent with the olivine CPO despite the low intragranular misorientation of both plagioclase and clinopyroxene (Figs 7a, b and 11) further points to refertilization by reactive percolation of melts coeval with deformation, with the CPO resulting from oriented crystallization and growth (e.g. Higgie & Tommasi, 2012, 2014; Tommasi et al., 2017). The contrast in composition of the products of the reactive melt percolation between the central/northern and southern massif corroborates that the high temperature, near-solidus deformation that formed the coarse-porphyroclastic foliation occurred in the spinel lherzolite stability field in the central and northern massifs, but in the plagioclase lherzolite stability field in the southern massif.

Thermobarometric estimates derived from core data in coarse-porphyroclastic peridotites of the southern massif (Fig. 14d, 1100–1150°C, 0.6–0.7 GPa) record equilibration at near solidus conditions at low pressure, consistently with the inferred synkinematic conditions. In contrast, thermobarometric estimates obtained using core data from coarse-porphyroclastic peridotites of the central massif (Fig. 14d, ~800°C, 0.8 GPa) correspond to subsolidus conditions, implying chemical re-equilibration of these peridotites at lower temperatures and pressures after the deformation that produced the pervasive coarse-porphyroclastic fabric and pyroxenitic layering. The less sinuous pyroxene and olivine grain boundaries in the coarse-porphyroclastic peridotites and websterite layers from the central and northern massifs (Fig. 6c) also point to subsolidus re-equilibration (annealing). These observations imply a time gap between the pervasive and localized deformations, during which the mantle volume that presently outcrops in the central and northern massifs was maintained at temperatures high enough to allow for effective solid-state diffusion. This contrasts with the continuous petrological and microstructural record in the southern massif.

The olivine CPO in coarse-porphyroclastic peridotites from all three massifs records deformation by dislocation creep with dominant activation of the [100](010) slip system (Fig. 11). The axial-[010] tendency of the olivine CPO (Fig. 10) may be explained by deformation in the presence of small melt fractions (Higgie & Tommasi, 2012, 2014). The CPO of the pyroxenes, which is often characterized by multiple maxima, with one coherent and others uncorrelated with the olivine CPO, implies that part of the pyroxenes formed prior to the deformation and part results from reactive melt percolation during or after the deformation. The intragranular deformation of the coarse orthopyroxene crystals

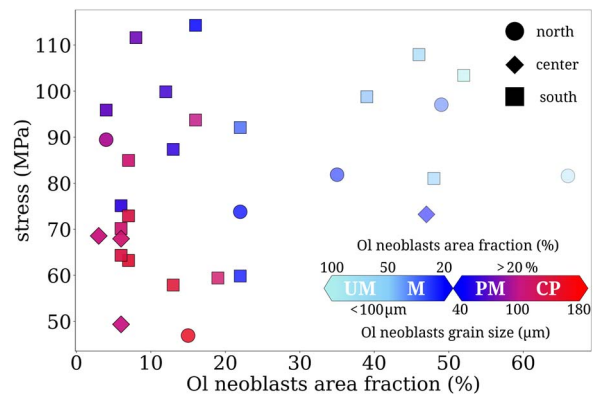


**Fig. 15.** Paleostresses determined based on the mean olivine neoblast equivalent grain size using the piezometer of Van Der Wal et al. (1993) for all studied peridotites.

indicates that these coarse grains are primary. The higher dispersion of the clinopyroxene CPO relative to the orthopyroxene may be explained by a higher fraction of secondary, melt-derived crystals.

Stresses associated with the pervasive deformation, estimated based on the arithmetic mean of the neoblast sizes of olivine and the Van Der Wal et al. (1993) piezometer, are in the range of 50–85 MPa, with a mean at 67 MPa (Fig. 15). No significant differences are observed between the southern and central/northern massifs, despite the higher temperature conditions of the deformation in the former. This result corroborates the conclusion from a previous study (Tommasi et al., 2017) that hydrous melts have a higher potential for producing softening than anhydrous melts (cf. constraints on the water contents of the melts present during the pervasive deformation in the thermodynamic modelling section below).

### Localized deformation—protomylonites, mylonites, and ultramylonites

The early stages of localized deformation, which are preserved in the protomylonites that compose the external domains of the shear zones, are characterized by the development of small volumes of a very fine-grained matrix forming a discontinuous anastomosed network at  $\pm 15^\circ$  on average to the elongation of the olivine porphyroclasts (Figs 5c, d and 6d). This matrix is produced by dynamic recrystallization of olivine, documented by the core-and-mantle structure of the olivine porphyroclasts (Figs 5c, d and 6d), but also by dissolution-precipitation processes, which are attested by the shapes of the orthopyroxene porphyroclasts and the asymmetric tails composed of intertwined fine-grained olivine and orthopyroxene that depart from them (Figs 5c, d and 6d). These dissolution-precipitation microstructures imply deformation in the presence of aqueous fluids (e.g. Hidas et al., 2016) or water-rich evolved melts (e.g. Frets et al., 2014; Tholen et al., 2023). The protomylonites display evidence for remobilization at the thin section scale of the existing phases, in particular orthopyroxene, and crystallization of minor amounts of amphibole (Figs 5c, d and 6d), but do not record any first-order change in bulk rock composition relative to the coarse-porphyroclastic peridotites other than hydration (Figs 4 and S3 in the supplementary material). This points to formation of the protomylonites in the presence of aqueous fluids, rather than melts. The nature of the fluid assisting



deformation will be further discussed in the next section, based on thermodynamic modelling. Although the neoblast sizes were not solely controlled by dynamic recrystallization, the decrease in olivine neoblast sizes (Fig. 3) suggests that the protomylonitic microstructure results from deformation under higher stresses (75–112 MPa with an average at 93 MPa, Fig. 15, Table S1) than the pervasive deformation that formed the coarse-porphyroclastic microstructures.

Progression of the localized deformation is recorded by a gradual increase in the matrix fraction in the mylonites and ultramylonites (Figs 3, 5e–i, and 8). Dislocation creep and dynamic recrystallization still play an essential role in the deformation of olivine, as documented by the further development of core-and-mantle structures (Figs 2, 5e–j, and 8a, c), the decrease in size and number of porphyroclasts (Fig. 9a), and the strong orientation relation between the neoblasts and porphyroclasts CPO (Fig. 10b). In the mylonites from the southern massif, plagioclase also recrystallizes dynamically. The increase in  $X_{Ca}$  of the neoblasts relative to the porphyroclasts (Figs 8d, 12e) records the decrease in confining pressure during the recrystallization (Fig. 14d).

Evidence for dissolution–precipitation and hydration reactions is omnipresent in the mylonites and ultramylonites. It encompasses (1) decrease in the size and increase in sinuosity of the boundaries (shape factor) of orthopyroxene porphyroclasts (Figs 5, 8, and 9a, c), (2) increase in the amount of fine-grained orthopyroxene, and to a lesser extent clinopyroxene, with interstitial or film-like habitus in the fine-grained mylonitic matrix and along recrystallized planes that crosscut obliquely, forming  $C'$  planes, the olivine porphyroclasts (Figs 2, 5e–i, and 8), and (3) increasing amphibole fractions that progressively replace clinopyroxene and plagioclase in the recrystallized matrix (Figs 2, 5e–i, and 8). The ultramylonites have almost no plagioclase and only relicts of clinopyroxene (Figs 4, 5i, j, and 8c). Plagioclase remains, nevertheless, a common phase both as porphyroclasts and neoblasts in the matrix in mylonites from the southern massif (Figs 4, 5e, 8c). Plagioclase also occurs as small grains rimming spinel in most mylonites from the central and northern massifs (Figs 5g and 8a). Dissolution and precipitation were also active during deformation at the brittle–ductile transition as attested by the fractures in olivine filled by fine-grained orthopyroxene in ultramylonite 85ZA71-13 (Fig. 8e).

The high Cl contents in amphibole in mylonitic peridotites equilibrated at temperatures of 800–900°C and pressures of 0.25–0.50 GPa (Figs 13d and 14d), which are up to four orders of magnitude higher than the usual concentrations in the mantle (Urann *et al.*, 2017), points to seawater ingress to >10 km depth. Lower Cl contents in late, post-kinematic amphiboles may be explained by the temperature dependence of Cl incorporation in amphibole (Campanaro & Jenkins, 2017). A similar evolution in Cl content in amphiboles, implying high-temperature deformation in the presence of seawater was previously documented in peridotites from transform faults (Prigent *et al.*, 2020).

Evolution from protomylonites to mylonites is accompanied by a minor, but not systematic decrease in the average sizes of olivine neoblasts and olivine neoblasts in the ultramylonites have similar average sizes as in the mylonites (Fig. 3). Although the olivine neoblast size in these rocks may have been modified by dissolution–precipitation processes, this implies that, despite the decrease in temperature and pressure conditions of the deformation, recorded by the data on rims and matrix grains of mylonites and ultramylonites (<500–850°C, 0.65–0.15 GPa,

Fig. 14d), and increasing strain localization, stresses did not increase, remaining below 110 MPa (Fig. 15).

Olivine CPOs in the mylonites and most ultramylonites (Fig. 11) corroborate that, despite the presence of fluids along grain boundaries, the activation of dissolution–precipitation processes, and the decreasing temperature conditions, olivine deformed by dislocation creep with dominant activation of the [100](010) slip system. The higher dispersion of the olivine CPO relative to that in the coarse-porphyroclastic peridotites and protomylonites (Fig. 10) is consistent with the increase in recrystallized fraction (e.g. Falus *et al.*, 2011). Only four amphibole-rich samples show CPO suggesting similar contributions of [100] and [001] glide to olivine deformation: mylonite 85ZA51 and ultramylonites 85ZA43b and 85ZA31b, in which olivine is almost completely recrystallized, and ultramylonite 85ZA71-13 in the southern massif, which displays evidence for deformation at the brittle–ductile transition (Fig. 8e). Ultramylonites 85ZA31b and 85ZA71-13 are characterized by maxima of [100] and [001] parallel to the lineation and to the maximum of [001] of amphibole (Fig. 11), suggesting activation of both [100](010) and [001](010). Ultramylonite 85ZA43b has [100] and [001] maxima normal to the amphibole [001] maximum (Fig. 11). However, the lineation in this ultramylonite is poorly defined.

The increase in the contribution of [001] glide to the deformation of olivine may result from an increase in stress due to decreasing temperature conditions (e.g. Durham & Goetze, 1977; Demouchy *et al.*, 2013). Incorporation of hydrogen in olivine as point defects may also favour [001] glide (e.g. Katayama *et al.*, 2004), but at much higher pressures and stresses than those inferred for the deformation of the Zabargad peridotites. Moreover, the hydrogen solubility in olivine at low pressures and temperature conditions is very low (Demouchy & Bolfan-Casanova, 2016; Padrón-Navarta & Hermann, 2017). Development of axial-[010] olivine CPO has also been documented in peridotites deformed in the presence of melts (Higgie & Tommasi, 2012, 2014) and in shear experiments on olivine + basalt systems (Holtzman *et al.*, 2003b). However, the PT conditions during the formation of the ultramylonites did not allow for the presence of melts (Fig. 14d). An alternative explanation is that the presence of a fluid phase along grain boundaries could also favour the alignment of the olivine [001] axis in the flow direction. Olivine CPO characterized by the alignment of [001] in the flow direction was indeed already described in ultramylonitic peridotites with similar dissolution–precipitation microstructures by Hidas *et al.* (2016). The fact that in the present study such olivine CPO are only observed in ultramylonites with high amphibole contents and almost no plagioclase suggests that instantaneous fluid fractions have to be rather high for this process to be activated.

The pyroxene CPO is more variable (Fig. 11). The parallelism between the pyroxenes [001] and the olivine [100] maxima suggests deformation by dislocation glide, consistently with the observed undulose extinction and, for the orthopyroxenes, elongation of the porphyroclasts in some mylonites. However, some mylonites and ultramylonites show pyroxene CPO with a concentration of [001], which is the only possible glide direction in pyroxenes (cf. Frets *et al.*, 2012 and references therein), at a high angle to the foliation. These CPO are similar to those described in peridotite mylonites and ultramylonites deformed in the presence of aqueous fluids by Hidas *et al.* (2016). In dissolution–precipitation creep, CPO development may be controlled by epitaxial growth. However, our data do not show any consistent orientation relation between olivine and pyroxenes

CPO. We cannot therefore propose a robust explanation for these 'abnormal' orthopyroxene CPO.

The plagioclase CPO in the mylonites and ultramylonites is much weaker and in most cases different from that in the coarse-porphroclastic peridotites. This change in CPO pattern is associated with the development of a marked substructure (polygonization) in the porphyroclasts, suggesting the activation of multiple slip systems and extensive dynamic recrystallization.

In conclusion, analysis of the microstructures and CPO in the mylonites and ultramylonites indicates that dislocation creep played an essential role in the deformation localized in the shear zones. It also documents that, except in the final stages of this deformation, which are recorded in the ultramylonites, olivine deformed by activating the same slip systems as during deformation in the asthenosphere or deep lithospheric mantle. Evidence for dissolution-precipitation processes, indicating local fluid saturation, is, nevertheless, omnipresent. Fluids played a major role in the mechanical behaviour of the peridotites in these shear zones. They (1) allowed deformation of the pyroxenes by dissolution-precipitation creep, (2) created, via dissolution-precipitation, a fine-grained polymineralic matrix in which grain growth will be hindered by pinning, and (3) lubricated the grain boundaries within this matrix. These fluid-assisted processes allowed for deformation to continue at decreasing temperature conditions and faster strain rates (localization implies accommodating the same displacement gradient in a smaller volume) without a major increase in stress. However, the fact that the olivine recrystallized fraction continuously increased until it represented ~50% of the olivine volume implies that dislocation creep remained important even in the ultramylonites. This suggests that instantaneous fluid fractions remained low and that grain size reduction did not suffice to produce a switch to a deformation dominated by grain boundary sliding. One may also speculate that dissolution-precipitation creep did not play a more important role in the deformation because of the limited incongruent dissolution of olivine and pyroxenes in aqueous fluids at temperatures <900°C (Newton & Manning, 2002; Macris *et al.*, 2020).

### Thermodynamic modelling: Constraints on the evolution of the PT conditions and melts or free fluids contents during deformation

To further constrain the composition and amount of fluids involved in the different stages of deformation, we conducted thermodynamic forward modelling. These models estimate the sequence of mineral reactions and changes in mineral composition based on a whole-rock analysis representative of the Zabargad peridotites (cf. Fig. S3). The models were computed under the assumption of thermodynamic equilibrium along idealized decompression and cooling paths, which were inferred based on estimates of the pressure-temperature evolution for (1) the southern massif and (2) the central and northern massifs (Fig. 14d). Therefore, the thermodynamic models predict hypothetical continuous trends in the evolution of mineral reactions and changes in mineral composition, rather than attempting to replicate the individual evolution of the diverse compositions observed in the Zabargad peridotites.

The challenge was to model an open system relative to the H<sub>2</sub>O component. Indeed, except for the water responsible for low amounts of high-Ti pargasite observed in the coarse-porphroclastic peridotites from the central and northern massifs, the petrostructural data in this study imply that externally derived aqueous fluids (here treated as external H<sub>2</sub>O influx)

have infiltrated the deforming peridotites either continuously or discontinuously during the decompression. Depending on the PT conditions, this external H<sub>2</sub>O influx could lead to reactions producing amphibole and consuming plagioclase and clinopyroxene until hydrous melting or saturation with an aqueous fluid was reached. The modelling assumes complete thermodynamic equilibrium with the external fluid, which is an assumption that is certainly not fulfilled in the natural system. Indeed, the preservation of core-to-rim compositional gradients, bimodal to multimodal grain size distributions, and contrasting microstructures at the thin section scale attests that complete equilibrium was never achieved. It was, at best, approached locally in the amphibole-rich ultramylonites, which record the last stages, most localized, of deformation. The thermodynamic simulations predict therefore minimum local instantaneous fluid contents.

The bulk rock composition of sample 85ZA37 was estimated based on modal abundances from EBSD mapping and average mineral chemical compositions from EPMA analyses (for comparison with bulk rock compositions of the other studied samples, cf. Table S2). Thermodynamic modelling was conducted using oxides with additional O<sub>2</sub> to account for potential redox reactions involving ferric iron. The amount of O<sub>2</sub> component was estimated based on the ferric iron content in spinel inferred by stoichiometry and the spinel modal abundance in 85ZA37, leading to a bulk oxidation state of iron rather conservative ( $\text{Fe}^{3+}/(\text{Fe}^{3+}+\text{Fe}^{2+})=0.033$  in atom proportions) when compared with that reported by Bonatti *et al.* (1986) and Piccardo *et al.* (1988), which ranges from 0.121 and 0.410 with an average of 0.213.

To account for the contrasting PT paths inferred for the southern massif and the central and northern massifs (Fig. 14d), pseudosections were computed along two different PT linear decompression and cooling trajectories (vertical axis in Fig. 16) for a system with variable H<sub>2</sub>O content: from strictly dry to 1.0 wt. % bulk H<sub>2</sub>O added to the bulk composition of sample 85ZA37 (horizontal axes in Fig. 16). Predictions for the evolution of modal and mineral compositions at equilibrium are then presented for nominally dry (200 ppm wt. H<sub>2</sub>O) decompression paths (full red and blue lines close to 0 wt.% in XH<sub>2</sub>O in Fig. 16) and two hydrous decompression paths (red and blue thick lines with a central white line in Fig. 16). These hydrous paths diverge from the nominally dry path at 1170°C for the northern and central massifs and 1100°C for the southern massif (first appearance of amphibole at near water-undersaturated solidus conditions). They are thereafter constrained by the water-saturated solidus down to ca. 950°C and 975°C for northern and central and southern massifs, respectively, and by the presence of a free aqueous fluid at lower temperatures (aqueous fluid saturation). In addition, for the southern massif, we also computed modal and mineral compositions at equilibrium for a melt/aqueous fluid undersaturated path along the near-zero mode of plagioclase (dashed red line in Fig. 16) to estimate the plagioclase composition just before its complete replacement.

The nominally dry PT paths correctly reproduce, for instance, the persistence of spinel in both peridotites and pyroxenites through the entire decompression path in the central and northern massifs and the occurrence of very coarse (mm-sized) spinel with plagioclase rims in the southern massif peridotites, suggesting that the southern history initially started in the spinel stability field at 0.9 GPa and temperatures around 1150°C (Fig. 16). In addition, the very high plagioclase content (up to 15%, but in most samples 5–8%) with clear synkinematic crystallization habitus implies nominally dry initial conditions in the southern



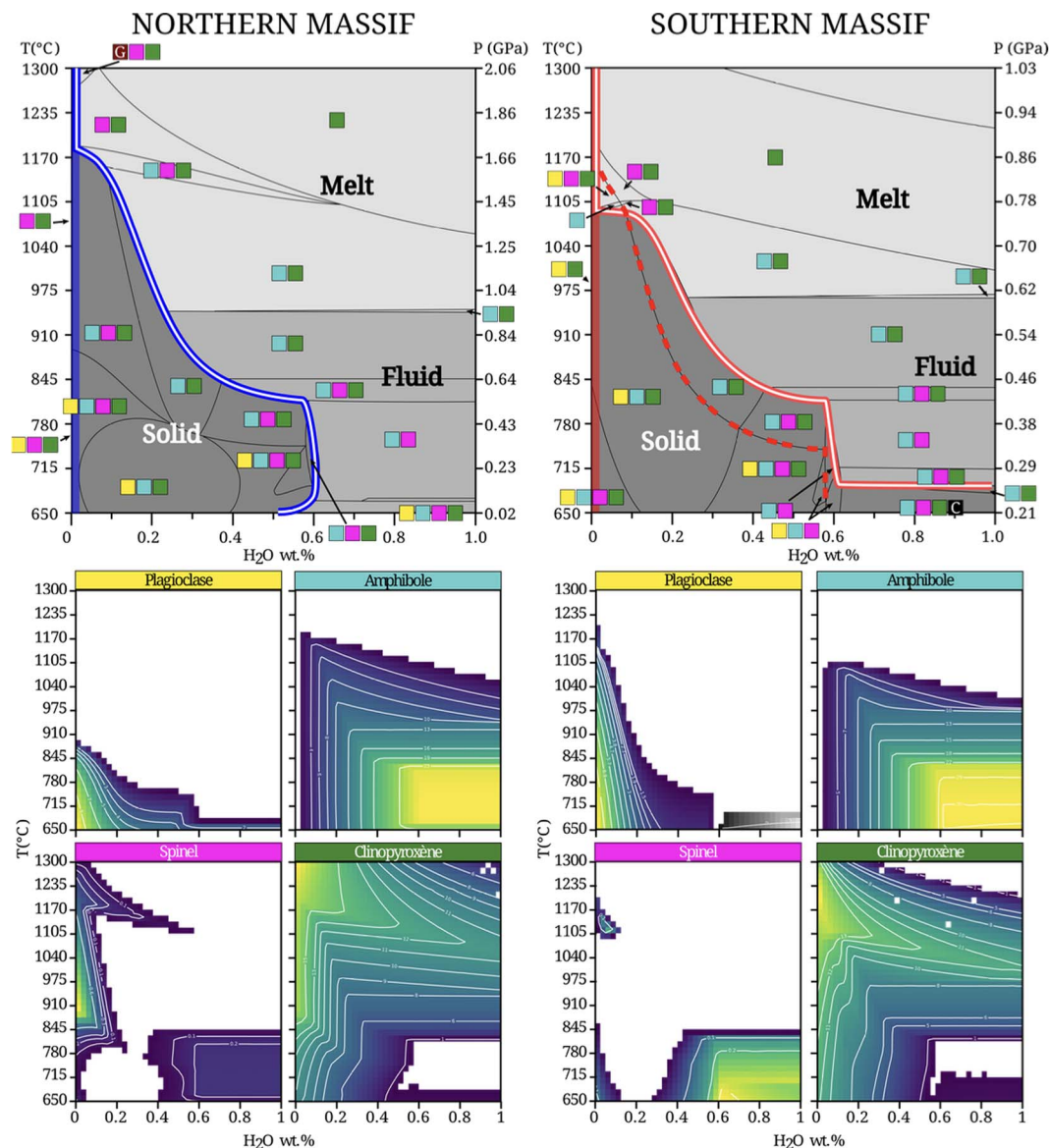


**Fig. 16.** Evolution of the system composition as a function of the water content ( $X_{H_2O}$  wt. %) for the PT paths inferred for the northern/central (left) and southern (right) massifs and the bulk rock composition of sample 85ZA37, chosen as representative of the average composition of the massif. The thick lines on the pseudosections indicate the paths used for calculating the evolution of mineral compositions during exhumation for the northern/central and southern massifs, respectively: the solid lines mark a nominally anhydrous path (200 ppm  $H_2O$ ), the double lines, a path following the melt or fluid saturation surface, and the dashed line, a melt/aqueous fluid undersaturated path along the near-zero mode of plagioclase. Coloured squares represent the stable modal composition of the solid matrix: Ol and Opx are not represented because they are stable over the entire field, for the other phases colours as in the phase maps: green = Cpx, yellow = Plg, cyan = Amph, purple = Sp. Garnet and chlorite, which are not observed in the studied peridotites, are indicated in brown and black, respectively. The panels below each pseudosection represent the stability field and variation in modal contents of the four Al-bearing phases. Grey contours in the bottom left of the plagioclase content panel for the southern massif document the stability field and evolution of the modal content of chlorite.

massif, since an external influx of only 0.1 wt.%  $H_2O$  at these conditions would have caused the complete disappearance of plagioclase (Fig. 16).

In contrast, the synkinematic crystallization of websterites in the central and northern massifs, which implies deformation at conditions close to the hydrous solidus, and the assemblages of ol + opx + cpx + sp + Ti-rich amphibole, with neither garnet nor garnet pseudomorphs in the coarse-porphyroclastic peridotites and websterites constrain the maximum initial conditions for the pervasive deformation at 1170°C and 1.5 GPa and a bulk  $H_2O$  content in the system of 0.2 wt. %. The occurrence of amphibole and high contents of orthopyroxene in the websteritic layers in the northern and central massifs support the hydrous nature of

the percolating melts. Comparison with experimental data (e.g. Lambart et al., 2012; Borghini et al., 2022) suggests also a high silica activity in the melts.

Departure from a nominally dry path and the presence of a free fluid phase during decompression and cooling are constrained by the microstructural evidence for fluid-assisted deformation. Thermodynamic simulations predict that, at equilibrium, the addition of external  $H_2O$  to the system systematically results in crystallization of amphibole, with complete replacement of plagioclase and Al-rich spinel by amphibole before reaching conditions at which a free melt or aqueous fluid may exist (Fig. 16). At temperatures below 840°C, fluid-saturation conditions require also the complete replacement of clinopyroxene, leaving

a mineral assemblage composed of olivine + amphibole + Cr-rich spinel. The preservation of coarse spinel rimmed by plagioclase and the persistence of plagioclase and clinopyroxene in the matrix of the mylonites and most ultramylonites requires therefore a spatially heterogeneous fluid distribution and probably also heterogeneity of the fluid flux through time, which prevented the reactions to go to completion while still allowing for widespread deformation by dissolution-precipitation. Equilibrium seems, nevertheless, to have been achieved in the ultramylonite 85ZA11, which contains 25 area % of amphibole, almost no clinopyroxene, and has spinel with high Cr contents. The appearance of Cr-rich spinel in the ultramylonites constrains the temperatures and pressures in the last deformation stages to  $<845^{\circ}\text{C}$  and  $<0.45$  GPa and requires instantaneous  $\text{H}_2\text{O}$  contents of at least 0.6 wt %. The absence of chlorite even in the most hydrated ultramylonites or in the peridotites deformed at the brittle–ductile transition constrains the minimum temperature of deformation to  $700^{\circ}\text{C}$  (Fig. 16).

The observed mineral chemistry trends are also in relatively good agreement with the thermodynamic modelling predictions (Fig. 17). However, the comparison between modelled and observed mineral compositions can only be conducted qualitatively. This limitation arises because thermodynamic models forecast equilibrium compositions, disregarding any kinetic effects, and do not account for bulk rock chemical fractionation resulting from partial or mosaic equilibrium in unreacted domains. Additionally, the Zabargad peridotites exhibit a considerable compositional range (cf. Figure 4 and Figs S1 and S3), whereas the models were based on a single bulk rock composition (that of sample 85ZA37 chosen to represent the average composition of the Zabargad peridotites).

Under nominally dry conditions, the evolution of orthopyroxene composition is strongly dependent on the decompression and cooling path followed. In contrast, if hydrous decompression paths were followed under complete equilibrium, orthopyroxenes from all three massifs should display similar compositional evolutions (Fig. 17a). The fact that different trends in Ca/Al ratios can still be observed (mostly in cores)—with high ratios in the southern massif and an almost constant low Ca content for a range of Al contents in the central and northern massifs—supports initial low  $\text{H}_2\text{O}$  contents and limited re-equilibration of the orthopyroxene porphyroclasts. The similar compositions of the rims and matrix orthopyroxenes in the three massifs are consistent with the predictions for hydrated systems. The weak decrease in  $X_{\text{Mg}}$  with decompression and hydration predicted by the models is probably masked in the observations by the variability in  $X_{\text{Mg}}$  among and within the samples (Fig. 17b). Both dry and water-saturated models do consistently predict, however, the observed increase in  $X_{\text{Mg}}$  and decrease in Al content in clinopyroxenes along the decompression and cooling paths (Fig. 17c). It is worth noting, however, that the most recent subsolidus models for orthopyroxene (clinopyroxene) from Tomlinson & Holland (2021) systematically overestimate (underestimate) the Al contents at all conditions relative to the present observations and also through direct comparison with the experimental data of Fumagalli *et al.* (2017). The same discrepancy is observed when previous supra-solidus models from Jennings & Holland (2015) and Holland *et al.* (2018) are used.

The observed progressive enrichment in the anorthite component in plagioclase during decompression and cooling (see also Fumagalli *et al.*, 2017) is also correctly modelled, but under nominally dry conditions  $X_{\text{Ca}}$  never reaches values higher than 0.78 (Fig. 17d). Hydrous models predict, however, significant

additional enrichment in  $X_{\text{Ca}}$  in response to fluid influx during exhumation (cf. Figure S4). Anorthitic plagioclases similar to that observed in the matrix of mylonites of the southern massif are predicted to be in equilibrium at temperatures  $\leq 850^{\circ}\text{C}$ , pressures  $\leq 0.45$  GPa, and 0.3–0.6 wt %  $\text{H}_2\text{O}$  (Figs 16 and 17d). However, under water-saturated conditions, at equilibrium, plagioclase should be fully replaced by amphibole for the entire central/northern path and between 1100 and  $700^{\circ}\text{C}$  for the southern path, leading to a gap in the predicted plagioclase anorthite content (Fig. 17d). This contrasts with the almost continuous increase in  $X_{\text{Ca}}$  in plagioclase observed in the Zabargad peridotites, which can be modelled if a melt/aqueous fluid undersaturated path along the near-zero mode of plagioclase (dashed red line in Fig. 17) is considered. Finally, the  $X_{\text{Ca}}$  values lower than 0.60 observed in coarse-porphyroclastic peridotites from the central massif (Fig. 17d) can only be modelled under nominally dry conditions if whole rock compositions with higher  $\text{Na}_2\text{O}/\text{CaO}$  ratios than that of sample 85ZA37 (such as the composition HNaFLZ in Fumagalli *et al.*, 2017) are considered. This change in whole rock composition would also increase the plagioclase maximum pressure stability to 0.9 GPa at  $1150^{\circ}\text{C}$ .

The thermodynamic models predict a stability gap and sharp increase in the Cr content and a decrease in  $X_{\text{Mg}}$  in spinel along the  $\text{H}_2\text{O}$  saturated decompression and cooling paths (Figs 16 and 17e). This compositional evolution is consistent with observations from all three massifs (Figs 12f and 17e). It is variably recorded among the samples, but all samples show a consistent enrichment of Cr content towards the rims. An outstanding case is recorded by mylonite 85ZA50, which displays the most extreme compositional core-rim variation (Fig. 12f). The observed increase in the Cr content and decrease in  $X_{\text{Mg}}$  in spinel may be explained by partial re-equilibration with amphibole in response to external fluid infiltration. Similar trends, but less extreme variations, have been documented in experiments on anhydrous systems, in response to re-equilibration under decreasing pressure conditions in the plagioclase stability field (Borghini *et al.*, 2010). Incomplete re-equilibration of the samples during the decompression and cooling paths may account for the absence of the spinel stability gap in the observations. Note that the spinel model from Tomlinson & Holland (2021) used in the present thermodynamic models successfully reproduces the Cr evolution trend, but fails to quantitatively reproduce the observed  $X_{\text{Mg}}$  range with the discrepancy enhanced at the highest Cr content. This failure might suggest a poor extrapolation of the spinel model to the low-temperature conditions inferred for these spinels ( $<840^{\circ}\text{C}$ ).

The  $\text{H}_2\text{O}$  saturated decompression and cooling models also reproduce the general observed trend from pargasite to tremolite-rich compositions reflected in the steady decrease in the amphibole occupancy of the A site ( $\text{Na} + \text{K}$ ) and the associated linear decrease in  $\text{Al}^{\text{IV}}$  with increasing hydration during decompression and cooling (Fig. 17f). However, the amphibole model of Green *et al.* (2016) used in the present study systematically overestimates the  $\text{Al}^{\text{IV}}$  content (Fig. 17f). The hydrous models also consistently predict a decrease in Ti content in amphibole with decreasing temperature, but the actual Ti contents are strongly dependent on the Ti content in the whole rock and on the amphibole modal content (Fig. 17g). Moreover, the amphiboles in Zabargad peridotites show first a decrease in Ti with only a minor increase in Si content and then an increase in Si (i.e. in the tremolite component) under constant low Ti content (compare Figs 14 and 17g). The amphibole model of Green *et al.* (2016), which, in contrast to the other models used in this work, was calibrated for mafic systems, is not able to reproduce this two-stage change in Ti vs. Si contents and predicts

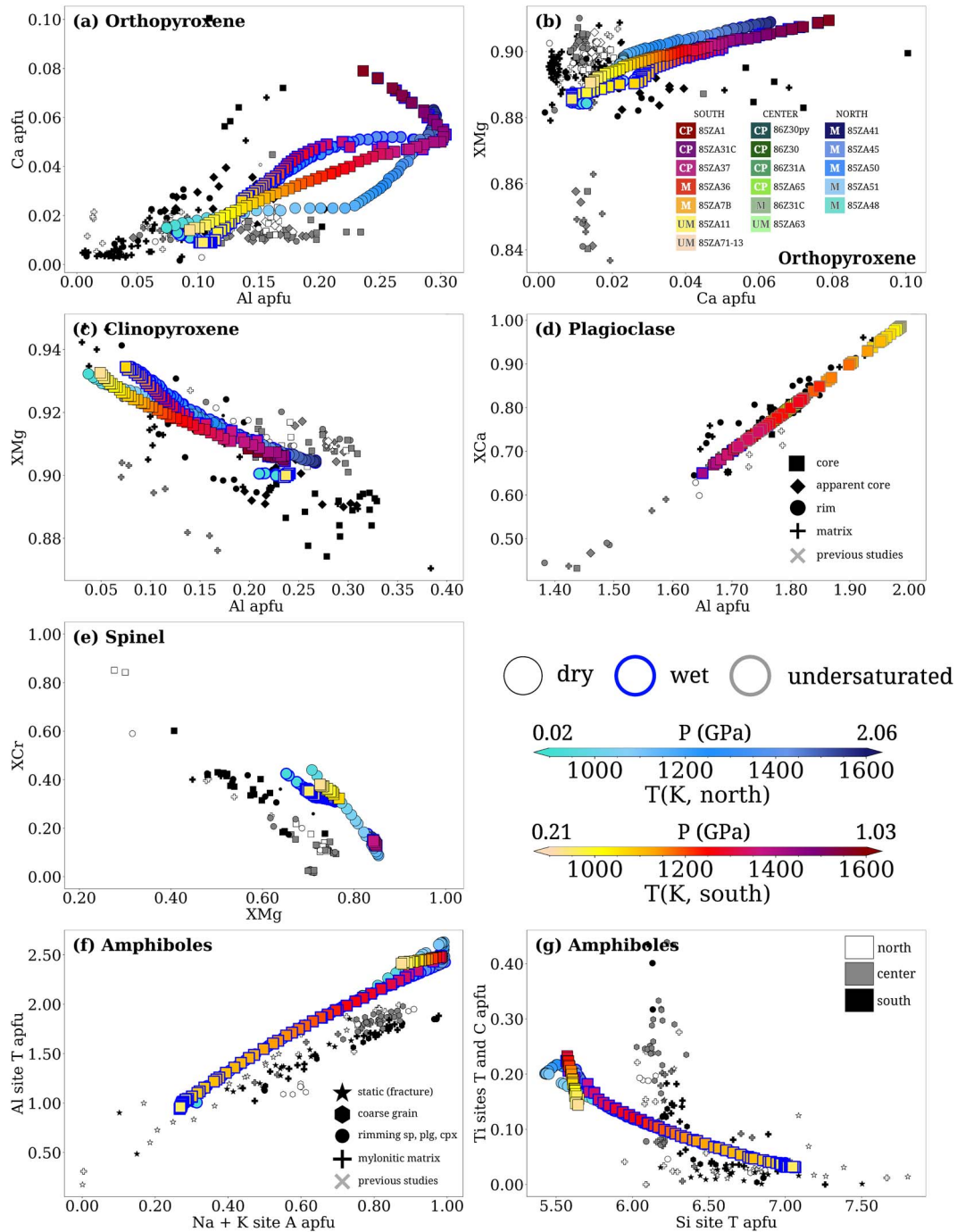


**Fig. 17.** Comparison between the mineral compositions predicted by the thermodynamical calculations for the five PT-hydration paths presented in Fig. 16 and those measured in the Zabargad peridotites. For the calculated compositions, the filling of the symbols indicates the evolution of equilibrium temperature and pressure (with warm colours for the south and cold colours for the north) and their contour, the nature of the path: black = nominally anhydrous and blue = melt or fluid-saturated. Circles contoured in grey in Fig. 17d indicate the evolution of  $X_{Ca}$  along the melt/aqueous fluid undersaturated path along the near-zero mode of plagioclase for the southern massif. For the measured data, symbols as in Figs. 12 and 13 with data from the southern massif in black, central massif in grey, and northern massif in white.

lower Si contents than the usual ones in pargasite (Fig. 17g) calling for new amphibole models for ultramafic compositions.

In summary, the thermodynamic models constrain: (1) initial pervasive (at the km scale) deformation in the presence of hydrous melts in the deep lithospheric mantle beneath a mature rift and dry melts in a shallow lithosphere-asthenosphere boundary in the rift-to-drift boundary, followed by (2) decompression and cooling concurrent with exhumation of mantle rocks by exten-

sional shear zones accompanied by infiltration of progressively larger amounts of externally derived aqueous fluids. Complete thermodynamic equilibrium with the external aqueous fluids was only achieved locally in a few ultramylonites, suggesting a spatially and temporally heterogeneous distribution of these fluids. Models for  $H_2O$ -saturated decompression and cooling paths qualitatively reproduce the observed evolution of orthopyroxene, clinopyroxene, plagioclase, spinel, and amphibole compositions.

Systematic discrepancies between modelled and observed compositions highlight, however, limitations in the presently available models for pyroxenes, spinel, and amphiboles in ultramafic systems. Inaccurate predictions regarding the composition of specific phases, even in minor amounts, will affect all phases, thereby partially explaining the limitations and discrepancies between the model and observation. Nonetheless, the incomplete equilibration and plagioclase metastability are even more critical in explaining the disparities between models and observations, as they involve chemically fractionating the volume of the metastable phase in the calculations, a factor not accounted for in the current models.

## Implications for the evolution of the Red Sea

The initial deformation in the central/northern and southern massifs records different stages of the rifting process. In both cases, the initial deformation occurred in the presence of melts and is pervasive at the hundreds of meters to the kilometer scale. However, the peridotites of the central and northern massifs record thinning of the subcontinental lithospheric mantle, with deformation initially assisted by reactive percolation of, first, hydrous melts (probably related to the Afar plume) and, later, aqueous fluids. The pervasive deformation occurred at temperatures of 1150–1180°C and pressures of 1.45–1.65 GPa (Figs 14 and 16) that is, at depths of 50–70 km in the subcontinental lithosphere, if one considers a 35 km-thick crust. Subsequent thinning and exhumation of this subcontinental lithospheric mantle by shearing in localized shear zones followed a steep, almost isothermal decompression path (Fig. 14d). This steep decompression path is consistent with that recorded by the lower crust gneisses in contact with the peridotites of the central massif (Boudier *et al.*, 1988; Seyler & Bonatti, 1988; Boullier *et al.*, 1997). The equilibrated textures of the coarse-porphyroclastic peridotites in these massifs may indicate a time gap between the pervasive and localized deformations, but it could also be explained by fast grain boundary migration, allowing for effective textural re-equilibration during the deformation in presence of hydrous melts (Tommasi *et al.*, 2017). In contrast, the peridotites of the southern massif record mantle exhumation in a more mature system, at the rift-to-drift transition. The pervasive deformation occurred in a shallow <30 km deep lithosphere–asthenosphere boundary, in the presence of melts produced by decompression upwelling in the asthenosphere. The subsequent exhumation of this lithosphere–asthenosphere boundary occurred along a path in which decompression is accompanied by fast cooling.

The final stages of mantle exhumation recorded in the shear zones in all three massifs are marked by an increasing contribution of fluids to the deformation, with significant contamination by sea water indicated by the high Cl contents of amphiboles in the mylonites (Fig. 13d), consistently with previous isotopic data by Agrinier *et al.* (1993) and the formation of Cl-rich scapolites in peridotites deformed at the brittle-ductile transition (Fig. 8f). The highest Cl contents were measured in amphiboles of mylonites equilibrated at temperatures of 800–900°C and pressures of 0.25–0.5 GPa, pointing to seawater ingress to >10 km depth. This channelling of surface fluids indicates that these shear zones crosscut the entire lithosphere, being connected to brittle faults that attained the surface. The equilibrium conditions recorded in the ultramylonites, including that preserving microstructures typical of deformation at the brittle to ductile transition, indicate that high geothermal gradients and hence that ductile deformation extended up to very shallow depths (700°C at <0.2 GPa, that is, ~6 km depth). These conditions are equivalent to those expected

under an active ridge. The presence of fluids and activation of fluid-assisted deformation processes allowed for increasingly localized deformation at decreasing temperatures at roughly constant stresses (Fig. 15). The presence of scapolite in the sample deformed at the brittle-ductile transition (Fig. 8f) suggests the presence of an evaporitic layer between the peridotites and the sea water during these last stages of deformation. Such a layer might have protected the exhumed peridotites from extensive reaction with seawater, explaining their exceptional freshness (almost complete absence of serpentine minerals).

## CONCLUSION

The present study documents thinning and exhumation of the mantle during continental rift and rift-to-drift transition accommodated in extensional shear zones. The petrostructural data of the Zabargad peridotites records both progressive strain localization and fluid-focusing in these extensional shear zones. The coupling of microstructural and petrological analyses enables documenting the whole exhumation history of mantle sections up to subsurface conditions at different stages of the rifting process. The central and northern massifs record an evolution starting at depths of 50–70 km in the subcontinental lithospheric mantle (1150–1180°C, 1.45–1.65 GPa) followed by a steep, almost isothermal decompression path. The southern massif represents a more mature system, at the rift-to-drift transition. Deformation started in a shallow <30 km deep lithosphere–asthenosphere boundary (1100–1200°C, 0.78–0.90 GPa), which was exhumed along a path in which decompression is accompanied by fast cooling.

The association of high-resolution cartography of the microstructure by EBSD with thermodynamic modelling documents the deformation of the olivine load-bearing framework of the peridotites essentially by dislocation creep, despite the evidence for the presence of, first, melts, and later, aqueous fluids within the extensional shear zones up to 10–15 km depth. The presence of fluids enabled activation of additional deformation processes, such as dissolution–precipitation, which (1) contributes to deformation by advective transport of matter along stress gradients, (2) reduces strain incompatibility by dissolving ortho- and clinopyroxene, which require higher stresses to deform by dislocation creep than olivine, (3) effectively reduces grain sizes by producing a well-mixed polymineralic fine-grained matrix. In addition, melts and fluids lubricate grain boundaries, enhancing grain boundary mobility and probably, locally, grain boundary sliding.

The similar olivine neoblast sizes in coarse-porphyroclastic peridotites in the southern and central/northern massif suggest that small fractions of hydrous melts have a higher softening potential than anhydrous melts. The decrease of olivine neoblast sizes from the coarse-porphyroclastic peridotites to the protomylonites suggests an increase in the peridotites strength associated with the transition from pervasive, melt-present to localized, fluid-assisted deformation, consistent with the decrease in temperature. On the other hand, the similar olivine neoblast sizes in the mylonites and ultramylonites indicate that the peridotites strength varied little despite the continued decrease in temperature conditions and localization of the deformation in smaller and smaller volumes. This observation indicates a progressive weakening of the rocks within the shear zones, a phenomenon we attribute to the growing involvement of fluids in the deformation process. However, the fact that the olivine recrystallized fraction continuously increased implies that dislocation creep remained important even in the ultramylonites, suggesting that



fluid-assisted processes alone did not suffice to accommodate the imposed deformation.

The thermodynamic models constrain that decompression and cooling are accompanied by infiltration of increasing amounts of externally derived aqueous fluids, which have a distinct seawater signature. However, the preservation of core-to-rim compositional gradients and, particularly, the preservation of plagioclase and clinopyroxene in the mylonites and to a lesser extent ultramylonites, suggests that complete thermodynamic equilibrium with the external fluid was likely never attained, except in a few ultramylonites. This implies spatially and probably temporally heterogeneous fluid distribution. Despite the limitations of representing the diversity of compositions with a single representative bulk composition and assuming instantaneous equilibrium, the models for H<sub>2</sub>O-saturated decompression and cooling paths successfully predict the general evolution trends for the orthopyroxene, clinopyroxene, plagioclase, and amphibole compositions shedding light on the hydration process during decompression and cooling. However, consistent discrepancies between modelled and observed compositions underscore the limitations of the current models for pyroxenes, spinel, and amphiboles in ultramafic systems.

## Acknowledgements

Françoise Boudier is warmly thanked for generously sharing the samples, photos, field notes, and her knowledge of the Zabargad peridotites. Alain Vauchez is thanked for the multiple discussions on deformation processes. Matthieu Zaderatzky collected the first set of EBSD as part of his Master's project at Université de Montpellier under the supervision of AT in 2015. Fabrice Barou, responsible for the EBSD platform at Geosciences Montpellier, acquired the detailed EBSD and EDS maps. We also thank Pierre Agrinier and Catherine Mevel for providing the entire amphibole microprobe dataset of Agrinier *et al.* (1993), as well as Christophe Nevado and Doriane Delmas, Olivia Mauguin, Romain Lafay and Anne Delplanque from Geosciences Montpellier, for the preparation of high-quality thin sections, assistance in the acquisition of the EPMA data, and producing the pseudosection figures, respectively.

## Funding

This work was supported by the European Research Council (ERC) under the European Union Horizon 2020 Research and Innovation programme [grant agreement No 882450 – ERC RhEoEVOLUTION].

## Data Availability

The data underlying this article are available in the article and in its online supplementary material.

## SUPPLEMENTARY MATERIAL

Supplementary data are available at Journal of Petrology online.

## REFERENCES

- Agrinier, P., Mével, C., Bosch, D. & Javoy, M. (1993). Metasomatic hydrous fluids in amphibole peridotites from Zabargad Island (Red Sea). *Earth and Planetary Science Letters* **120**, 187–205. [https://doi.org/10.1016/0012-821X\(93\)90239-6](https://doi.org/10.1016/0012-821X(93)90239-6).
- Bachmann, F., Hielscher, R. & Schaeben, H. (2010). Texture analysis with MTEX – free and open source software toolbox. *Solid State Phenomena* **160**, 63–68. <https://doi.org/10.4028/www.scientific.net/SSP.160.63>.
- Bachmann, F., Hielscher, R. & Schaeben, H. (2011). Grain detection from 2d and 3d EBSD data—specification of the MTEX algorithm. *Ultramicroscopy* **111**, 1720–1733. <https://doi.org/10.1016/j.ultramic.2011.08.002>.
- Boillot, G., Recq, M., Winterer, E. L., Meyer, A. W., Applegate, J., Baltuck, M., Bergen, J. A., Comas, M. C., Davies, T. A., Dunham, K., Evans, C. A., Girardeau, J., Goldberg, G., Haggerty, J., Jansa, L. F., Johnson, J. A., Kasahara, J., Loreau, J. P., Luna-Sierra, E., Moullade, M., Ogg, J., Sarti, M., Thurow, J. & Williamson, M. (1987). Tectonic denudation of the upper mantle along passive margins: a model based on drilling results (ODP leg 103, western Galicia margin, Spain). *Tectonophysics* **132**, 335–342. [https://doi.org/10.1016/0040-1951\(87\)90352-0](https://doi.org/10.1016/0040-1951(87)90352-0).
- Bonatti, E., Clocchiatti, R., Colantoni, P., Gelmini, R., Marinelli, G., Ottonello, G., Santacroce, R., Taviani, M., Abdel-Meguid, A. A., Assaf, H. S. & el Tahir, M. A. (1983). Zabargad (St. John's) Island: an uplifted fragment of sub-Red Sea lithosphere. *Journal of the Geological Society* **140**, 677–690. <https://doi.org/10.1144/gsjgs.140.4.0677>.
- Bonatti, E., Ottonello, G. & Hamlyn, P. R. (1986). Peridotites from the island of Zabargad (St. John), Red Sea: petrology and geochemistry. *Journal of Geophysical Research* **91**, 599–631. <https://doi.org/10.1029/JB091iB01p00599>.
- Borghini, G., Fumagalli, P. & Rampone, E. (2010). The stability of plagioclase in the upper mantle: subsolidus experiments on fertile and depleted lherzolite. *Journal of Petrology* **51**, 229–254. <https://doi.org/10.1093/petrology/egp079>.
- Boudier, F., Nicolas, A., Ji, S., Kienast, J. R. & Mevel, C. (1988). The gneiss of Zabargad Island: deep crust of a rift. *Tectonophysics* **150**, 209–227. [https://doi.org/10.1016/0040-1951\(88\)90302-2](https://doi.org/10.1016/0040-1951(88)90302-2).
- Boullier, A.-M., Firdaous, K. & Boudier, F. (1997). Fluid circulation related to deformation in the Zabargad gneisses (Red Sea rift). *Tectonophysics* **279**, 281–302. [https://doi.org/10.1016/S0040-1951\(97\)00116-9](https://doi.org/10.1016/S0040-1951(97)00116-9).
- Brey, G. P. & Köhler, T. (1990). Geothermobarometry in four-phase Lherzolites II. New Thermobarometers, and practical assessment of existing Thermobarometers. *Journal of Petrology* **31**, 1353–1378. <https://doi.org/10.1093/petrology/31.6.1353>.
- Brune, S., Kolawole, F., Olive, J.-A., Stamps, D. S., Buck, W. R., Buiters, S. J. H., Furman, T. & Shillington, D. J. (2023). Geodynamics of continental rift initiation and evolution. *Nature Reviews Earth & Environment* **4**, 235–253. <https://doi.org/10.1038/s43017-023-00391-3>.
- Bunge (1982) *Texture Analysis in Materials Science: Mathematical Methods*. Amsterdam: Elsevier. ISBN: 9780408106429
- Campanaro, B. P. & Jenkins, D. M. (2017). An experimental study of chlorine incorporation in amphibole synthesized along the pargasite–ferro-pargasite join. *Canadian Mineralogist* **55**, 419–436. <https://doi.org/10.3749/canmin.1600082>.
- Connolly, J. A. D. (2005). Computation of phase equilibria by linear programming: a tool for geodynamic modeling and its application to subduction zone decarbonation. *Earth and Planetary Science Letters* **236**, 524–541. <https://doi.org/10.1016/j.epsl.2005.04.033>.
- Connolly, J. A. D. (2009). The geodynamic equation of state: what and how. *Geochemistry, Geophysics, Geosystems* **10**, 2009GC002540. <https://doi.org/10.1029/2009GC002540>.
- Dean, S. L., Sawyer, D. S. & Morgan, J. K. (2015). Galicia Bank ocean–continent transition zone: new seismic reflection constraints. *Earth and Planetary Science Letters* **413**, 197–207.
- Demouchy, S. & Bolfan-Casanova, N. (2016). Distribution and transport of hydrogen in the lithospheric mantle: a review. *Lithos* **240–243**, 402–425. <https://doi.org/10.1016/j.lithos.2015.11.012>.

- Demouchy, S., Tommasi, A., Boffa Ballaran, T. & Cordier, P. (2013). Low strength of Earth's uppermost mantle inferred from tri-axial deformation experiments on dry olivine crystals. *Physics of the Earth and Planetary Interiors* **220**, 37–49. <https://doi.org/10.1016/j.pepi.2013.04.008>.
- Dupuy, C., Mével, C., Bodinier, J.-L. & Savoyant, L. (1991). Zabargad peridotite: evidence for multistage metasomatism during Red Sea rifting. *Geology* **19**, 722. [https://doi.org/10.1130/0091-7613\(1991\)019<#x003C;0722:ZPEFMM>#x003E;2.3.CO;2](https://doi.org/10.1130/0091-7613(1991)019<#x003C;0722:ZPEFMM>#x003E;2.3.CO;2).
- Durham, W. B. & Goetze, C. (1977). Plastic flow of oriented single crystals of olivine: 1. Mechanical data. *Journal of Geophysical Research* **82**, 5737–5753. <https://doi.org/10.1029/JB082i036p05737>.
- Falus, G., Tommasi, A. & Soustelle, V. (2011). The effect of dynamic recrystallization on olivine crystal preferred orientations in mantle xenoliths deformed under varied stress conditions. *Journal of Structural Geology* **33**, 1528–1540. <https://doi.org/10.1016/j.jsg.2011.09.010>.
- Frets, E., Tommasi, A., Garrido, C. J., Padrón-Navarta, J. A., Amri, I. & Targuisti, K. (2012). Deformation processes and rheology of pyroxenites under lithospheric mantle conditions. *Journal of Structural Geology* **39**, 138–157. <https://doi.org/10.1016/j.jsg.2012.02.019>.
- Frets, E. C., Tommasi, A., Garrido, C. J., Vauchez, A., Mainprice, D., Targuisti, K. & Amri, I. (2014). The Beni Bousera peridotite (Rif Belt, Morocco): an oblique-slip low-angle shear zone thinning the subcontinental mantle lithosphere. *Journal of Petrology* **55**, 283–313. <https://doi.org/10.1093/petrology/egt067>.
- Fumagalli, P., Borghini, G., Rampone, E. & Poli, S. (2017). Experimental calibration of Forsterite–Anorthite–Ca–Tschermak–enstatite (FACE) geobarometer for mantle peridotites. *Contributions to Mineralogy and Petrology* **172**, 38. <https://doi.org/10.1007/s00410-017-1352-2>.
- Green, E. C. R., White, R. W., Diener, J. F. A., Powell, R., Holland, T. J. B. & Palin, R. M. (2016). Activity–composition relations for the calculation of partial melting equilibria in metabasic rocks. *Journal of Metamorphic Geology* **34**, 845–869. <https://doi.org/10.1111/jmg.12211>.
- Hidas, K., Tommasi, A., Garrido, C. J., Padrón-Navarta, J. A., Mainprice, D., Vauchez, A., Barou, F. & Marchesi, C. (2016). Fluid-assisted strain localization in the shallow subcontinental lithospheric mantle. *Lithos* **262**, 636–650. <https://doi.org/10.1016/j.lithos.2016.07.038>.
- Higgie, K. & Tommasi, A. (2012). Feedbacks between deformation and melt distribution in the crust–mantle transition zone of the Oman ophiolite. *Earth and Planetary Science Letters* **359–360**, 61–72. <https://doi.org/10.1016/j.epsl.2012.10.003>.
- Higgie, K. & Tommasi, A. (2014). Deformation in a partially molten mantle: constraints from plagioclase lherzolites from Lanzo, western Alps. *Tectonophysics* **615–616**, 167–181. <https://doi.org/10.1016/j.tecto.2014.01.007>.
- Holland, T. J. B. & Powell, R. (2011). An improved and extended internally consistent thermodynamic dataset for phases of petrological interest, involving a new equation of state for solids: thermodynamic dataset for phases of petrological interest. *Journal of Metamorphic Geology* **29**, 333–383. <https://doi.org/10.1111/j.1525-1314.2010.00923.x>.
- Holland, T. J. B., Green, E. C. R. & Powell, R. (2018). Melting of peridotites through to granites: a simple thermodynamic model in the system KNCFMASHTOCr. *Journal of Petrology* **59**, 881–900. <https://doi.org/10.1093/petrology/egy048>.
- Holland, T. J. B., Green, E. C. R. & Powell, R. (2022). A thermodynamic model for feldspars in  $\text{KAlSi}_3\text{O}_8$ – $\text{NaAlSi}_3\text{O}_8$ – $\text{CaAl}_2\text{Si}_2\text{O}_8$  for mineral equilibrium calculations. *Journal of Metamorphic Geology* **40**, 587–600. <https://doi.org/10.1111/jmg.12639>.
- Holtzman, B. K., Groebner, N. J., Zimmerman, M. E., Ginsberg, S. B. & Kohlstedt, D. L. (2003a). Stress-driven melt segregation in partially molten rocks. *Geochemistry, Geophysics, Geosystems* **4**, 2001GC000258. <https://doi.org/10.1029/2001GC000258>.
- Holtzman, B. K., Kohlstedt, D. L., Zimmerman, M. E., Heidelbach, F., Hiraga, T. & Hustoft, J. (2003b). Melt segregation and strain partitioning: implications for seismic anisotropy and mantle flow. *Science* **301**, 1227–1230. <https://doi.org/10.1126/science.1087132>.
- Jennings, E. S. & Holland, T. J. B. (2015). A simple thermodynamic model for melting of peridotite in the system NCFMASOCr. *Journal of Petrology* **56**, 869–892. <https://doi.org/10.1093/petrology/egv020>.
- Katayama, I., Jung, H. & Karato, S. (2004). New type of olivine fabric from deformation experiments at modest water content and low stress. *Geology* **32**, 1045. <https://doi.org/10.1130/G20805.1>.
- Lambart, S., Laporte, D., Provost, A. & Schiano, P. (2012). Fate of pyroxenite-derived melts in the peridotitic mantle: thermodynamic and experimental constraints. *Journal of Petrology* **53**, 451–476.
- Li, X., Zhang, C., Behrens, H. & Holtz, F. (2020). Calculating amphibole formula from electron microprobe analysis data using a machine learning method based on principal components regression. *Lithos* **362–363**, 105506. <https://doi.org/10.1016/j.lithos.2020.105506>.
- Macris, C. A., Newton, R. C., Wykes, J., Pan, R. & Manning, C. E. (2020). Diopside, enstatite and forsterite solubilities in H<sub>2</sub>O and H<sub>2</sub>O–NaCl solutions at lower crustal and upper mantle conditions. *Geochimica et Cosmochimica Acta* **279**, 119–142. <https://doi.org/10.1016/j.gca.2020.03.035>.
- Mainprice, D., Bachmann, F., Hielscher, R. & Schaeben, H. (2015). Descriptive tools for the analysis of texture projects with large datasets using MTEX : strength, symmetry and components. *Geological Society, London, Special Publications* **409**, 251–271. <https://doi.org/10.1144/SP409.8>.
- McKenzie, D. (1978). Some remarks on the development of sedimentary basins. *Earth and Planetary Science Letters* **40**, 25–32. [https://doi.org/10.1016/0012-821X\(78\)90071-7](https://doi.org/10.1016/0012-821X(78)90071-7).
- Newton, R. C. & Manning, C. E. (2002). Solubility of enstatite + forsterite in H<sub>2</sub>O at deep crust/upper mantle conditions: 4 to 15 kbar and 700 to 900°C. *Geochimica et Cosmochimica Acta* **66**, 4165–4176. [https://doi.org/10.1016/S0016-7037\(02\)00998-5](https://doi.org/10.1016/S0016-7037(02)00998-5).
- Nicolas, A., Boudier, F. & Montigny, R. (1987). Structure of Zabargad Island and early rifting of the Red Sea. *Journal of Geophysical Research* **92**, 461–474. <https://doi.org/10.1029/JB092iB01p00461>.
- Nimis, P. & Grütter, H. (2010). Internally consistent geothermometers for garnet peridotites and pyroxenites. *Contributions to Mineralogy and Petrology* **159**, 411–427. <https://doi.org/10.1007/s00410-009-0455-9>.
- Ozawa, K. & Takahashi, N. (1995). PT history of a mantle diapir: the Horoman peridotite complex, Hokkaido, northern Japan. *Contributions to Mineralogy and Petrology* **120**, 223–248.
- Padrón-Navarta, J. A. & Hermann, J. (2017). A subsolidus olivine water solubility equation for the Earth's upper mantle. *Journal of Geophysical Research: Solid Earth* **122**, 9862–9880.
- Piccardo, G. B., Messiga, B. & Vannucci, R. (1988). The Zabargad peridotite–pyroxenite association: petrological constraints on its evolution. *Tectonophysics* **150**, 135–162. [https://doi.org/10.1016/0040-1951\(88\)90299-5](https://doi.org/10.1016/0040-1951(88)90299-5).
- Prigent, C., Warren, J. M., Kohli, A. H. & Teyssier, C. (2020). Fracture-mediated deep seawater flow and mantle hydration on oceanic transform faults. *Earth and Planetary Science Letters* **532**, 115988. <https://doi.org/10.1016/j.epsl.2019.115988>.



- Seyler, M. & Bonatti, E. (1988). Petrology of a gneiss-amphibolite lower crustal unit from Zabargad Island, Red Sea. *Tectonophysics* **150**, 177–207. [https://doi.org/10.1016/0040-1951\(88\)90301-0](https://doi.org/10.1016/0040-1951(88)90301-0).
- Taylor, W. R. (1998). An experimental test of some geothermometer and geobarometer formulations for upper mantle peridotites with application to the thermobarometry of fertile lherzolite and garnet websterite. *N Jb Min Abh* **172**, 381–408.
- Tholen, S., Linckens, J. & Zulauf, G. (2023). Melt-enhanced strain localization and phase mixing in a large-scale mantle shear zone (Ronda peridotite, Spain). *Solid Earth* **14**, 1123–1154. <https://doi.org/10.5194/se-14-1123-2023>.
- Tomlinson, E. L. & Holland, T. J. B. (2021). A thermodynamic model for the subsolidus evolution and melting of peridotite. *Journal of Petrology* **62**, egab012. <https://doi.org/10.1093/petrology/egab012>.
- Tommasi, A. & Vauchez, A. (2015). Heterogeneity and anisotropy in the lithospheric mantle. *Tectonophysics* **661**, 11–37. <https://doi.org/10.1016/j.tecto.2015.07.026>.
- Tommasi, A., Langone, A., Padrón-Navarta, J. A., Zanetti, A. & Vauchez, A. (2017). Hydrous melts weaken the mantle, crystallization of pargasite and phlogopite does not: insights from a petrostructural study of the Finero peridotites, southern Alps. *Earth and Planetary Science Letters* **477**, 59–72. <https://doi.org/10.1016/j.epsl.2017.08.015>.
- Urann, B. M., Le Roux, V., Hammond, K., Marschall, H. R., Lee, C.-T. A. & Monteleone, B. D. (2017). Fluorine and chlorine in mantle minerals and the halogen budget of the Earth's mantle. *Contributions to Mineralogy and Petrology* **172**, 51. <https://doi.org/10.1007/s00410-017-1368-7>.
- Van Der Wal, D., Chopra, P., Drury, M. & Gerald, J. F. (1993). Relationships between dynamically recrystallized grain size and deformation conditions in experimentally deformed olivine rocks. *Geophysical Research Letters* **20**, 1479–1482. <https://doi.org/10.1029/93GL01382>.
- Weinberg, R. F., Regenauer-Lieb, K. & Rosenbaum, G. (2007). Mantle detachment faults and the breakup of cold continental lithosphere. *Geology* **35**, 1035. <https://doi.org/10.1130/G23918A.1>.
- Wernicke, B. (1981). Low-angle normal faults in the basin and Range Province: nappe tectonics in an extending orogen. *Nature* **291**, 645–648. <https://doi.org/10.1038/291645a0>.
- White, R. W., Powell, R. & Johnson, T. E. (2014). The effect of Mn on mineral stability in metapelites revisited: new  $a - x$  relations for manganese-bearing minerals. *Journal of Metamorphic Geology* **32**, 809–828. <https://doi.org/10.1111/jmg.12095>.
- Whitmarsh, R. B., Manatschal, G. & Minshull, T. A. (2001). Evolution of magma-poor continental margins from rifting to seafloor spreading. *Nature* **413**, 150–154. <https://doi.org/10.1038/35093085>.
- Witt-Eickchen, G. & Seck, H. A. (1991). Solubility of Ca and Al in orthopyroxene from spinel peridotite: an improved version of an empirical geothermometer. *Contributions to Mineralogy and Petrology* **106**, 431–439. <https://doi.org/10.1007/BF00321986>.